Cell Reports

Article

Mutant FUS and ELAVL4 (HuD) Aberrant Crosstalk in Amyotrophic Lateral Sclerosis

Graphical Abstract

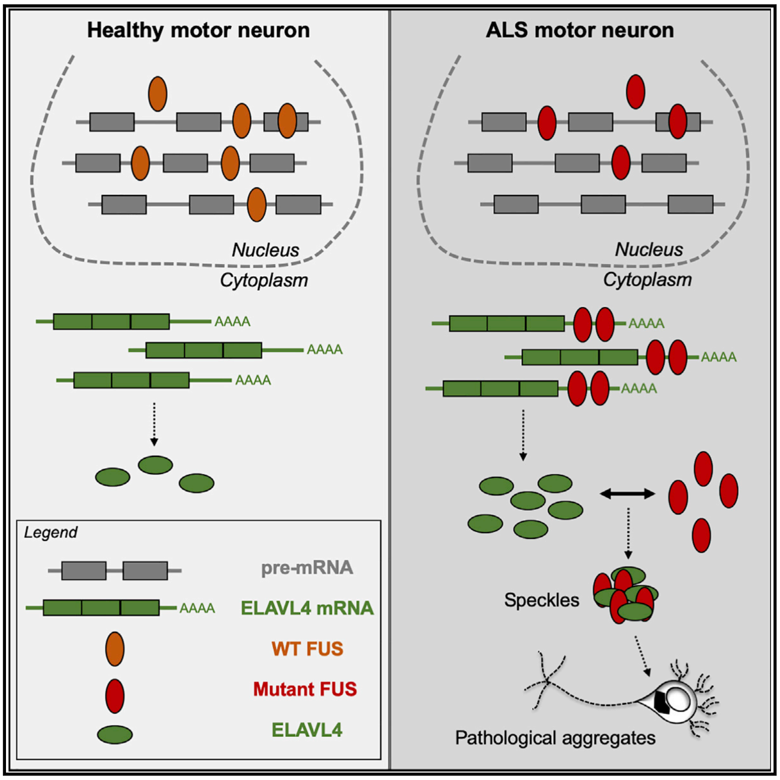

Highlights

- We report the RNA interactome of wild-type and mutant FUS in human motor neurons
- Mutant FUS binds the mRNA 3′ UTR of other RNA-binding proteins, including ELAVL4
- ELAVL4, expressed at increased levels, interacts with mutant FUS in the cytoplasm
- ELAVL4 proteinopathy occurs in both FUS ALS and in sporadic ALS patients

Authors

Riccardo De Santis, Vincenzo Alfano, Valeria de Turris, ..., R. Jeroen Pasterkamp, Irene Bozzoni, Alessandro Rosa

Correspondence

alessandro.rosa@uniroma1.it

In Brief

De Santis et al. show that the mutant RNA-binding protein FUS, linked to amyotrophic lateral sclerosis (ALS), targets other RNA-binding proteins, such as ELAVL4, in human motor neurons. This triggers aberrant crosstalk between mutant FUS and ELAVL4, which is found in pathological inclusions of ALS patients' motor neurons.

De Santis et al., 2019, Cell Reports *27*, 3818–3831
June 25, 2019 © 2019 The Author(s).
https://doi.org/10.1016/j.celrep.2019.05.085

Cell Reports
Article

Mutant FUS and ELAVL4 (HuD) Aberrant Crosstalk in Amyotrophic Lateral Sclerosis

Riccardo De Santis,[1,2,7,8] Vincenzo Alfano,[2,7,9] Valeria de Turris,[1] Alessio Colantoni,[2] Laura Santini,[2,10]
Maria Giovanna Garone,[2] Giuseppe Antonacci,[1,11] Giovanna Peruzzi,[1] Emma Sudria-Lopez,[3] Emanuel Wyler,[4]
Jasper J. Anink,[5] Eleonora Aronica,[5] Markus Landthaler,[4,6] R. Jeroen Pasterkamp,[3] Irene Bozzoni,[1,2]
and Alessandro Rosa[1,2,12,*]
[1]Center for Life Nano Science, Istituto Italiano di Tecnologia, Viale Regina Elena 291, 00161 Rome, Italy
[2]Department of Biology and Biotechnology Charles Darwin, Sapienza University of Rome, P.le A. Moro 5, 00185 Rome, Italy
[3]Department of Translational Neuroscience, UMC Utrecht Brain Center, University Medical Center Utrecht, Utrecht University, Universiteitsweg 100, 3584 CG Utrecht, the Netherlands
[4]Berlin Institute for Medical Systems Biology, Max-Delbrück-Center for Molecular Medicine in the Helmholtz Association, Robert-Rössle-Strasse 10, 13125 Berlin, Germany
[5]Amsterdam UMC, University of Amsterdam, Department of (Neuro)Pathology, Amsterdam Neuroscience, Meibergdreef 9, 1105 AZ Amsterdam, the Netherlands
[6]IRI Life Sciences, Institute für Biologie, Humboldt Universität zu Berlin, Philippstraße 13, 10115 Berlin, Germany
[7]These authors contributed equally
[8]Present address: Laboratory of Stem Cell Biology and Molecular Embryology, The Rockefeller University, New York, NY 10065, USA
[9]Present address: Cancer Research Center of Lyon (CRCL) UMR INSERM 1052-CNRS 5286 151 cours Albert Thomas, 69424 Lyon Cedex 03, France
[10]Present address: Department of Microbiology, Immunobiology and Genetics, Center for Molecular Biology of the University of Vienna, Max F. Perutz Laboratories, Vienna Biocenter (VBC), 1030 Vienna, Austria
[11]Present address: Photonics Research Group, Ghent University-IMEC, Technologiepark-Zwijnaarde 126, 9052 Ghent, Belgium
[12]Lead Contact
*Correspondence: alessandro.rosa@uniroma1.it

https://doi.org/10.1016/j.celrep.2019.05.085

SUMMARY

Amyotrophic lateral sclerosis (ALS) has been genetically linked to mutations in RNA-binding proteins (RBPs), including FUS. Here, we report the RNA interactome of wild-type and mutant FUS in human motor neurons (MNs). This analysis identified a number of RNA targets. Whereas the wild-type protein preferentially binds introns, the ALS mutation causes a shift toward 3′ UTRs. Neural ELAV-like RBPs are among mutant FUS targets. As a result, ELAVL4 protein levels are increased in mutant MNs. ELAVL4 and mutant FUS interact and co-localize in cytoplasmic speckles with altered biomechanical properties. Upon oxidative stress, ELAVL4 and mutant FUS are engaged in stress granules. In the spinal cord of FUS ALS patients, ELAVL4 represents a neural-specific component of FUS-positive cytoplasmic aggregates, whereas in sporadic patients it co-localizes with phosphorylated TDP-43-positive inclusions. We propose that pathological mutations in FUS trigger an aberrant crosstalk with ELAVL4 with implications for ALS.

INTRODUCTION

RNA-binding proteins (RBPs) play multiple roles in the processing, localization, and function of RNA molecules, in both nuclear and cytoplasmic compartments (Gerstberger et al., 2014). Dysregulation of RNA metabolism has been proposed as a key underlying element in neurodegenerative disorders (Gao and Taylor 2014). Amyotrophic lateral sclerosis (ALS) is a disease primarily caused by the degeneration of motor neurons (MNs) and is genetically linked to mutations in several RBPs, including FUS (also known as TLS) and TDP-43 (Lagier-Tourenne et al., 2010). Cytoplasmic inclusions of mutated proteins have been reported in the brain and spinal cord of FUS and TDP-43 patients (Kwiatkowski et al., 2009; Vance et al., 2009; Yokoseki et al., 2008; Van Deerlin et al., 2008). FUS is a shuttling protein endowed with a nuclear export signal and a nuclear localization signal. It is mainly localized in the nucleus, but notably, several pathogenic mutations associated to ALS cluster in the C-terminal nuclear localization signal (PY domain), resulting in defects in nuclear import (Deng et al., 2014). Thus, nuclear exclusion and aberrant cytoplasmic localization of the mutated protein have been proposed as the initial step in ALS pathogenesis (Bentmann et al., 2013). Both the loss of a nuclear function and the gain of a possibly toxic function in the cytoplasm have been proposed as pathological mechanisms contributing to ALS (Ling et al., 2013). RBPs are often found in membraneless organelles, variously referred to as bodies, granules, or speckles, assembled by a process of liquid-liquid phase separation mediated by low-complexity domains (Courchaine et al., 2016). Interestingly, FUS-positive cytoplasmic inclusions found in ALS patients contain proteins normally present in stress granules (SGs), such as PABP and eIF4G (Dormann et al., 2010). SGs are membraneless transitory structures containing ribonucleoproteins (RNPs) and serving as temporary storage compartments for mRNAs during stress conditions (Anderson and Kedersha, 2009). Conversely, cytoplasmic inclusions are stable and highly insoluble. It is currently unknown how pathological FUS-positive aggregates form in patients' cells. It has been proposed that chronic stress and/or other genetic risk factors might promote the conversion of transient SGs into stable inclusion bodies (Dormann and Haass, 2011; Wolozin 2012), possibly by a liquid-to-solid phase transition of mutant FUS (Patel et al., 2015).

FUS plays multiple roles both in the nucleus and in the cytoplasm. In the nucleus, FUS participates in the regulation of alternative splicing by interacting with nascent transcripts (Ishigaki et al., 2012; Rogelj et al., 2012; Lagier-Tourenne et al., 2012; Nakaya et al., 2013; Zhou et al., 2013). Accordingly, preferential binding of endogenous wild-type FUS to intronic regions was reported in mouse and human brain (Ishigaki et al., 2012; Rogelj et al., 2012; Lagier-Tourenne et al., 2012; Nakaya et al., 2013). Interestingly, genes with long introns and encoding for proteins involved in neuronal integrity were found among common targets of FUS and TDP-43 (Lagier-Tourenne et al., 2012). FUS also regulates splicing of its own mRNA by binding to exon 7 and its flanking introns as a feedback mechanism to control FUS protein levels in the cell (Zhou et al., 2013; Dini-Modigliani et al., 2014). Moreover, FUS regulates splicing of other RBPs by binding to their conserved introns (Nakaya et al., 2013; Masuda et al., 2015). In addition to alternative splicing, nuclear FUS regulates mRNA length by binding alternative polyadenylation sites of nascent RNA (Masuda et al., 2015). Selective analysis of the cytoplasmic targets of endogenous FUS in mouse NSC-34 motoneuronal-like cells provided evidence for 3′ UTR binding in this compartment (Colombrita et al., 2012). This is consistent with the physiological role of FUS in transporting mRNAs for local translation in neuronal cells and promoting mRNA stability (Fujii et al., 2005; Udagawa et al., 2015; Yokoi et al., 2017). The toxic gain-of-function effects of ALS-associated mutations may be partly due to increased interaction with cytoplasmic RNA targets. Mutant FLAG-hemagglutinin (HA)-tagged transgenic FUS expressed in HEK293 cells showed an altered binding profile: wild-type FUS mostly associated with introns, whereas mutant FUS proteins bound predominantly to 3′ UTRs (Hoell et al., 2011). This shift in the bound region on the target transcripts is consistent with the altered subcellular localization of the mutated protein because the proportion of introns is much lower in the cytoplasmic compared to the nuclear transcriptome.

The reasons of selective MN vulnerability downstream of FUS mutations remain currently unknown. FUS is ubiquitously expressed and ALS-linked mutations cause its mislocalization in any cell type, including regions of the nervous system spared by the disease. Human induced pluripotent stem cells (iPSCs) provide the opportunity of addressing the cellular and molecular bases of selective MN death in ALS (Sances et al., 2016). We have recently generated and characterized FUS mutant iPSCs, which can be converted into MNs along with isogenic wild-type controls (Lenzi et al., 2015; De Santis et al., 2017). In mutant iPSC-derived MNs, FUS is de-localized in the cytoplasm, as expected, and we described alterations in the transcriptome and microRNA pathways. However, mutant FUS may alter cellular functions without affecting RNA levels, for instance by mislocalizing bound transcripts and/or dysregulating their translation. Which transcripts are targeted by mutant FUS in human MNs and what are the effects of aberrant FUS binding on these RNAs in the cytoplasm remain currently unknown. So far, studies aimed at characterizing FUS target transcripts have been performed on the wild-type protein (Colombrita et al., 2012; Ishigaki et al., 2012; Rogelj et al., 2012; Lagier-Tourenne et al., 2012; Nakaya et al., 2013; Zhou et al., 2013; Masuda et al., 2015). The only exception is represented by the work of Hoell et al. (2011) in which mutant FUS proteins were ectopically expressed in HEK293 cells. Notably, a number of target genes perturbed by FUS depletion in neuronal cells are not expressed in non-neuronal cell lines (Lagier-Tourenne et al., 2012).

Here, we filled this gap of information about the RNA interactome of mutant FUS in MNs by performing photoactivatable ribonucleoside-enhanced crosslinking and immunoprecipitation (PAR-CLIP) analysis in human iPSC-derived motor neurons. A systematic comparison of the binding patterns of wild-type and mutant (P525L) FUS showed that the ALS mutation causes a major shift in FUS partners. Interestingly, genes encoding for RBPs were identified among transcripts bound in the 3′ UTR by mutant FUS. We focused on the neural-specific RBP ELAVL4 (HuD), which we previously showed to be indirectly regulated by FUS via the microRNA miR-375 (De Santis et al., 2017). Here, we found that mutant FUS binds *ELAVL4* 3′ UTR, resulting in increased production of the ELAVL4 protein. The ELAVL4 protein localizes in stiff cytoplasmic granules and interacts with mutant FUS proteins. Speckles containing both proteins are formed upon mutant FUS and ELAVL4 expression at non-physiological levels. Such speckles are distinct from SGs; however, ELAVL4 and mutant FUS co-localize in SGs upon oxidative stress, pointing to ELAVL4 as a SG component in human MNs. Finally, ELAVL4 was found in cytoplasmic aggregates in the spinal cord of ALS patients. We propose a model in which mutant FUS/ELAVL4 speckles might represent pathological ALS aggregates precursors, partly explaining the neuro-specific toxicity FUS mutations.

RESULTS

Wild-Type and Mutant FUS RNA Interactors in Human MNs

Human iPSCs carrying the P525L mutation in both *FUS* alleles (hereafter FUS^{P525L}) and their isogenic *FUS* wild-type control (hereafter FUS^{WT}) (Lenzi et al., 2015) were differentiated into spinal MNs by using a previously established protocol (De Santis et al., 2017) (Figure S1A). The P525L mutation, linked to a severe and juvenile form of ALS, impairs the transportin-mediated nuclear import of FUS by disrupting the interaction with the transport pathway (Dormann et al., 2010). As a consequence, FUS partially de-localized into the cytoplasm in FUS^{P525L} MNs (Figure 1A; Figures S1B–S1D). We performed PAR-CLIP (Hafner et al., 2010) on both FUS^{WT} and FUS^{P525L} MN populations. Immunoprecipitation of crosslinked RNA-protein complexes by using a FUS antibody resulted in a prominent radioactive band at the expected molecular weight, for both FUS^{WT} and FUS^{P525L} (Figure 1B). We additionally generated PAR-CLIP libraries in MN

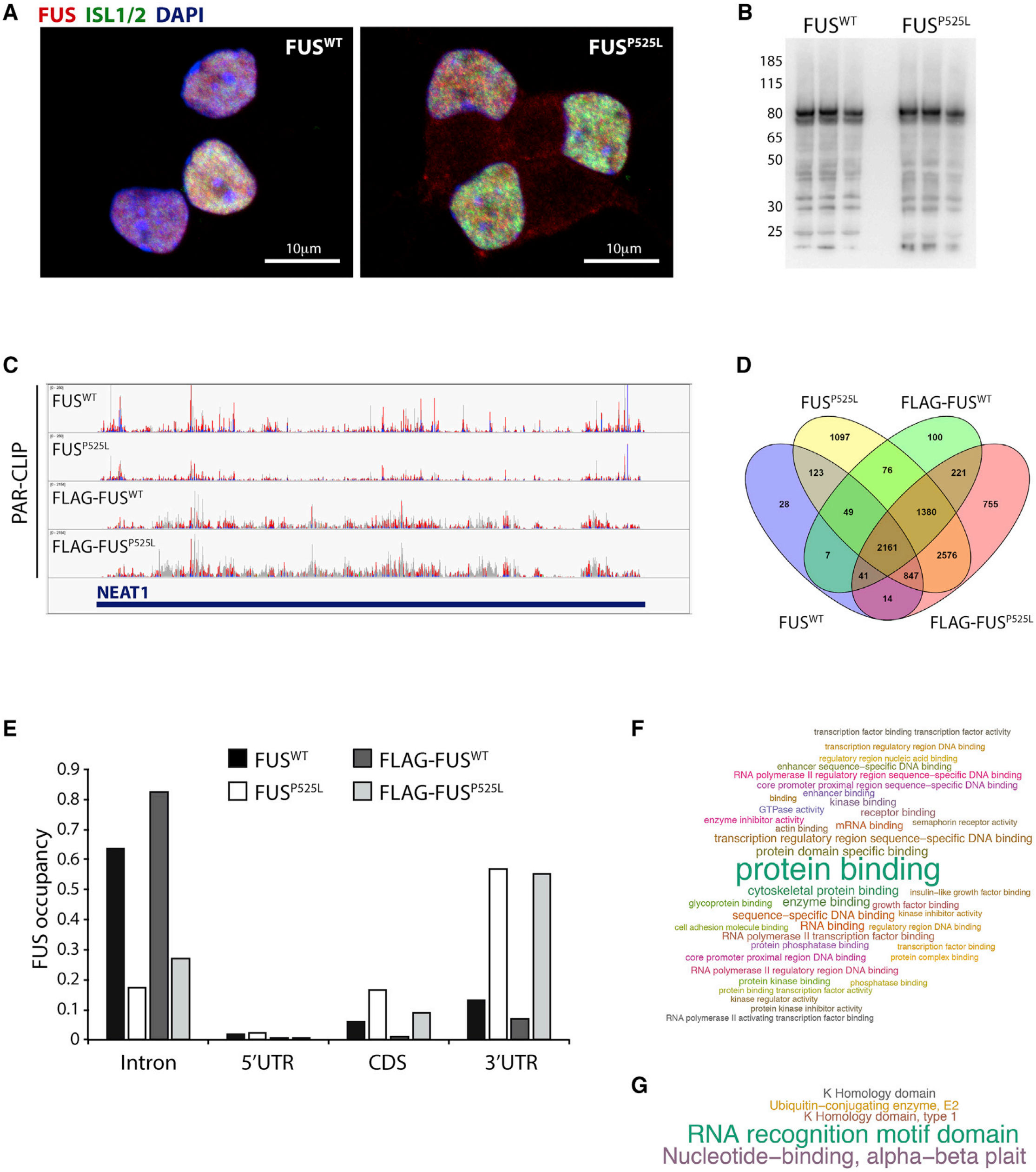

Figure 1. Identification of RNA Targets of FUS$^{\mathrm{WT}}$ and FUS$^{\mathrm{P525L}}$ in Human iPSC-Derived Motor Neurons by PAR-CLIP

(A) Immunostaining showing FUS localization (red) in fluorescence-activated cell sorting (FACS)-purified MNs (day 12+7, see Figure S1A). ISL1/2 (green) marks MNs and 4′,6-diamidino-2-phenylindole (DAPI; blue) the nuclei. Scale bars, 10 µm. Single channels are shown in Figure S1B.

(B) Autoradiograph image of crosslinked RNA immunoprecipitated with an anti-FUS antibody, 5′ end radiolabeled, and separated by SDS-PAGE. Numbers indicate the molecular weight (kDa).

(C) Snapshot of the Integrative Genomics Viewer (IGV) window showing the mapping of PAR-CLIP reads and transitions on the NEAT1 locus.

(D) Venn diagram of overlapping targets with at least one T-C transition in the mature transcript in the indicated PAR-CLIP datasets.

(E) The histogram shows the percentage of T-C transitions occurring in the PAR-CLIP datasets across different regions of the MN transcriptome (introns, 5′ UTR, coding sequence [CDS], and 3′ UTR).

(F and G) Word cloud generated by FIDEA representing GO Molecular Functions (F) and InterPro (G) terms enriched in the set of FUS$^{\mathrm{P525L}}$ 3′ UTR-bound targets. The categories are represented with a character size proportional to the statistical significance of their enrichment.

See also Figures S1 and S2.

populations that ectopically express a FLAG-tagged version of either wild-type or P525L mutant FUS (Figures S1E–S1G). These independent PAR-CLIP libraries were used to avoid possible biases due to antibody aspecificity. Detection of binding sites in previously described FUS interactors, such as the long noncoding RNA *NEAT1*, *FUS* intron 7, and *EWSR* (Lagier-Tourenne et al., 2012; Nishimoto et al., 2013), technically validated our results (Figure 1C; Figure S1H).

We interrogated our PAR-CLIP dataset to assess whether FUS mutant protein binds different mRNAs compared to FUS^{WT}. We identified 3270 FUS^{WT}, 8309 FUS^{P525L}, 4035 FLAG-FUS^{WT}, and 7995 FLAG-FUS^{P525L} protein-coding targets with at least one thymidine to cytidine transition (T-C; revealing the crosslinked site in the PAR-CLIP analysis) in the mature transcript (Table S1). A subset of transcripts is bound by mutant FUS only (Figure 1D). We then analyzed the percentage of T-C occurring in the different pre-mRNA and mature mRNA regions (introns, coding sequences and 5′ and 3′ UTRs). Wild-type FUS is mostly bound to intronic regions, confirming previous reports (Hoell et al., 2011; Rogelj et al., 2012; Lagier-Tourenne et al., 2012; Nakaya et al., 2013; Masuda et al., 2015). Conversely, FUS mutant protein preferentially binds the 3′ UTR (Figure 1E). Because the FUS^{P525L} protein was partially de-localized in the cytoplasm, reduced binding to intronic regions was expected. Moreover, our findings are in agreement with a previously reported PAR-CLIP dataset from HEK293 cells expressing FUS^{R521G}, showing preferential binding of the mutant protein to 3′ UTR (Hoell et al., 2011). Seeking for pathways possibly affected by mutant FUS 3′ UTR binding, we performed Gene Ontology (GO) term enrichment analysis using the Functional Interpretation of Differential Expression Analysis (FIDEA) tool (D'Andrea et al., 2013). Several GO terms cooperating in distinct pathways and molecular functions were found to be significantly enriched (Figures 1F and 1G; Figure S2A). Among them, we noticed categories related to "protein binding-mRNA binding-RNA binding" in the molecular functions. Moreover, focusing on the INTERPRO categories, we found an enrichment of the "RNA recognition motif domain" protein domain category (Figure 1G). Notably, GO analysis performed on targets with more than 10% of T-C transitions in the 3′ UTR showed enrichment of categories related to RNA metabolism (Figures S2B and S2C). We next crossed the PAR-CLIP data with the RNA sequencing (RNA-seq) results previously obtained from FUS^{WT} and FUS^{P525L} MNs (De Santis et al., 2017). We assessed the fraction of differentially expressed genes in MNs carrying the FUS^{P525L} mutation that are bound by FUS^{wt} and/or FUS^{P525L} in our PAR-CLIP dataset. This analysis resulted in significant enrichment for FUS-bound mRNAs among those that are not differentially expressed in MNs (Figure S2D), suggesting that, globally, the ALS mutation does not induce a change in RNA levels of FUS direct targets. Compared to a dataset of wild-type FUS targets previously obtained by CLIP-seq in human brain cortex (Lagier-Tourenne et al., 2012), our analysis revealed a number of targets, among motor-neuron-expressed genes, bound by wild-type or mutant FUS only, or both (Figure S2E).

Collectively, these data show that FUS^{wt} and FUS^{P525L} have a different profile of mRNAs targets, with a drift of the mutant protein toward 3′ UTR binding.

FUS Regulates ELAVL4 Expression by Binding the 3′ UTR of Its mRNA

Because functional enrichment analysis of mutant FUS-bound genes highlighted categories related to RNA metabolism, such as "RNA binding" and "RNA recognition domain," we focused our attention on RBPs encoded by those genes. Among them, we noticed three RBPs belonging to the Hu-embryonic lethal abnormal vision-like (ELAVL) family: *ELAVL2*, *ELAVL3*, and *ELAVL4* (also known as *HuB*, *HuC*, and *HuD*, respectively). In the PAR-CLIP datasets, their 3′ UTR displayed a strong enrichment of binding sites of mutant FUS compared to the wild-type (Figure 2A; Figure S3A). In our previous work, we showed that *ELAVL4* transcript levels were increased in FUS mutant MNs compared to their isogenic WT controls and that such aberrant upregulation could be partially ascribed to decreased levels of miR-375 (De Santis et al., 2017). We assessed the functional consequences of the interaction between mutant FUS and selected 3′ UTRs by taking advantage of a reconstituted system, consisting of HeLa cells ectopically expressing a FUS transgene fused to the red fluorescent protein (RFP) by inducible piggyBac-based vectors (Figure 2B). As expected, RFP-FUS^{WT} was localized in the nucleus, whereas RFP-FUS^{P525L} showed a strong cytoplasmic de-localization. This experimental set up allowed systematic evaluation of the effect of FUS binding in the absence of miR-375, which is not expressed in HeLa (Figures S3B and S3C). Reporter constructs containing genes of interest 3′ UTR fused with the luciferase coding sequence were transfected in HeLa cells expressing RFP-FUS^{WT}, RFP-FUS^{P525L}, or RFP as a control. We observed increased activity of the reporter containing the *ELAVL4* 3′ UTR in the presence of RFP-FUS^{P525L}, as compared to both RFP alone and RFP-FUS^{WT} (Figure 2C). Notably, similar outcomes were observed for the other two ELAVL family members. Conversely, no effect of either mutant or wild-type FUS was observed on the vector devoid of any 3′ UTR (empty vector) or in the presence of the 3′ UTR of an unrelated gene, *PPP1R15A*, which was also among the genes bound by mutant FUS in their 3′ UTR (Table S1). We focused our attention on *ELAVL4* 3 ′UTR to investigate whether the increase of reporter activity could be due to mRNA stabilization. We quantified by real-time qRT-PCR the relative levels of reporter mRNA in all conditions, showing a slight upregulation in RFP-FUS^{P525L} HeLa cells compared to RFP control and a minimal difference with RFP-FUS^{WT} (Figure 2D), suggesting that mutant FUS might increase *ELAVL4* expression at the level of translation and, in minor part, mRNA stability.

We then measured *ELAVL4* protein and mRNA levels in human iPSC-derived MNs, at different time points of differentiation (Figure S1A). Expression of *ELAVL4* was significantly upregulated in FUS^{P525L} MNs compared to isogenic controls (Figures 2E and 2F). Together with our previous work (De Santis et al., 2017), these results suggest that increased ELAVL4 levels in mutant MNs might result from both indirect (miR-375-mediated) and direct (3′UTR-binding-mediated) activities of mutant FUS.

ELAVL4 and Mutant FUS Co-localize in Cytoplasmic Granules

We next aimed at characterizing the consequences of ELAVL4 protein expression beyond physiological levels and its interaction

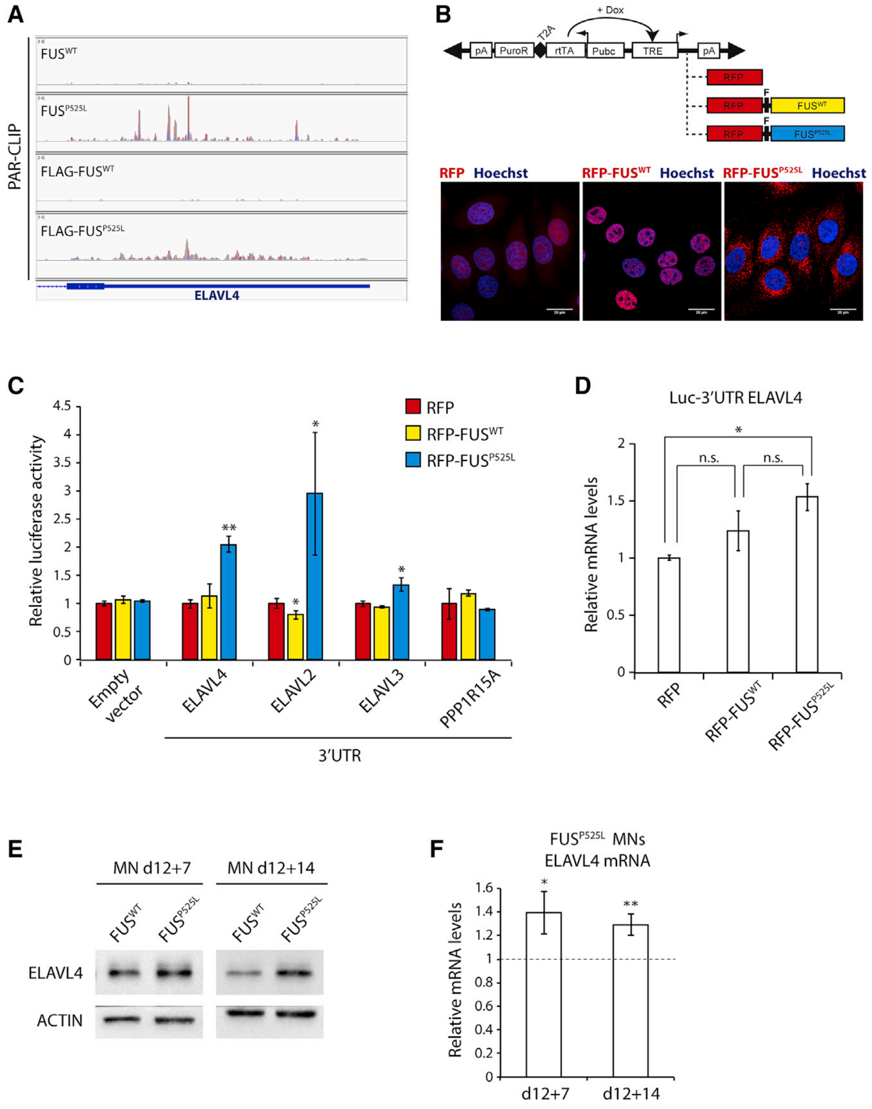

Figure 2. FUS^{P525L} Binds and Regulates the ELAVL4 3′ UTR

(A) Snapshot of the IGV window showing the mapping of PAR-CLIP reads and transitions on the *ELAVL4* 3′UTR.

(B) Upper panel, schematic representation of the enhanced piggyBac transposable vector for doxycycline conditional expression of RFP-FUS^{WT} (epB-Puro-TT-RFP-FUS^{WT}), RFP-FUS^{P525L} (epB-Puro-TT-RFP-FUS^{P525L}), and RFP control (epB-Puro-TT-RFP). F, FLAG tag; pA, polyadenylation signal; PuroR, puromycin resistance gene; T2A, self-cleavage peptide; rtTA, TET transactivator protein gene; Pubc, human ubiquitin C constitutive promoter; TRE, TET responsive element; Dox, doxycycline. Triangles represent terminal repeats of the transposon. Lower panels, HeLa cells expressing RFP, RFP-FUS^{WT}, RFP-FUS^{P525L} (red) and stained with Hoechst (blue) for nuclei. Scale bars, 20 μm.

(C) Luciferase assay on selected target 3′ UTRs in HeLa cells expressing RFP, RFP-FUS^{WT}, and RFP-FUS^{P525L}.

(D) Measurement of the RNA levels of the Luciferase-ELAVL4-3′UTR by real time qRT-PCR (relative expression compared to RFP-transfected cells). Histogram bars represent the average of 3 independent experiments and error bars indicate the SD (Student's t test; paired; two tails; $^*p < 0.05$; n.s., $p > 0.05$).

(E) ELAVL4 protein quantification by western blot in FUS^{WT} and FUS^{P525L} FACS-purified MNs at two different time points of differentiation (see Figure S1A).

(F) ELAVL4 RNA levels were measured by real time qRT-PCR. Expression levels in FUS^{P525L} MNs are shown as relative to the isogenic FUS^{WT} control, set to a value of 1 (dashed bar). Histogram bars represent the average of 3 independent experiments and error bars indicate the SD (Student's t test; paired; two tails; $^*p < 0.05$; $^{**}p < 0.01$).

See also Figure S3.

with mutant FUS. The coding sequence of *ELAVL4* was cloned in frame with a GFP reporter in the inducible piggyBac vector (Figure 3A), and GFP-ELAVL4 was ectopically expressed in HeLa cells. In the cytoplasmic compartment, we observed a diffuse localization punctuated by bright speckles (Figure 3B, left and middle panels) or more concentrated perinuclearly (Figure 3B, right panel). Co-staining with the SG marker PABP suggested that ELAVL4-positive speckles were not SGs (Figure S4A).

Direct protein-protein interaction between ELAVL4 and wild-type FUS has been recently reported (Blokhuis et al., 2016; Yokoi et al., 2017). As wild-type FUS is almost exclusively localized in the nucleus, such interaction presumably occurs in this compartment. The primary consequence of ALS mutations in the PY domain is the de-localization of FUS in the cytoplasm. We wondered whether mutant FUS de-localization, coupled with increased ELAVL4 levels, might alter FUS/ELAVL4 behavior. To assess the consequences of ELAVL4 increased expression in the presence of FUS^{P525L}, we took advantage of double reporter HeLa cell lines ectopically expressing GFP-ELAVL4 and RFP-FUS (either wild-type or P525L mutant) upon doxycycline induction (Figures 2B and 3A). Although RFP-FUS^{WT} maintained nuclear localization, confocal microscopy images show a high degree of co-localization of GFP-ELAVL4 and RFP-FUS^{P525L} in cytoplasmic speckles (Figure 3C). Interestingly, the co-expression of mutant FUS caused a marked increase of ELAVL4 levels in the speckles, which appeared bigger in size. Also in this case, double-positive mutant FUS^{P525L}/ELAVL4 speckles do not represent SGs (Figures S4B and S4C).

We have recently developed a non-contact and label-free imaging method, named background-deflection Brillouin (BDB) microscopy, to investigate the three-dimensional intracellular biomechanical properties of whole cells at a sub-micron resolution (Antonacci et al., 2018). Combined with confocal fluorescent microscopy, this technique provides a measure of the stiffness and viscoelastic properties of subcellular compartments (Scarcelli et. al., 2015; Antonacci and Braakman, 2016). HeLa cells

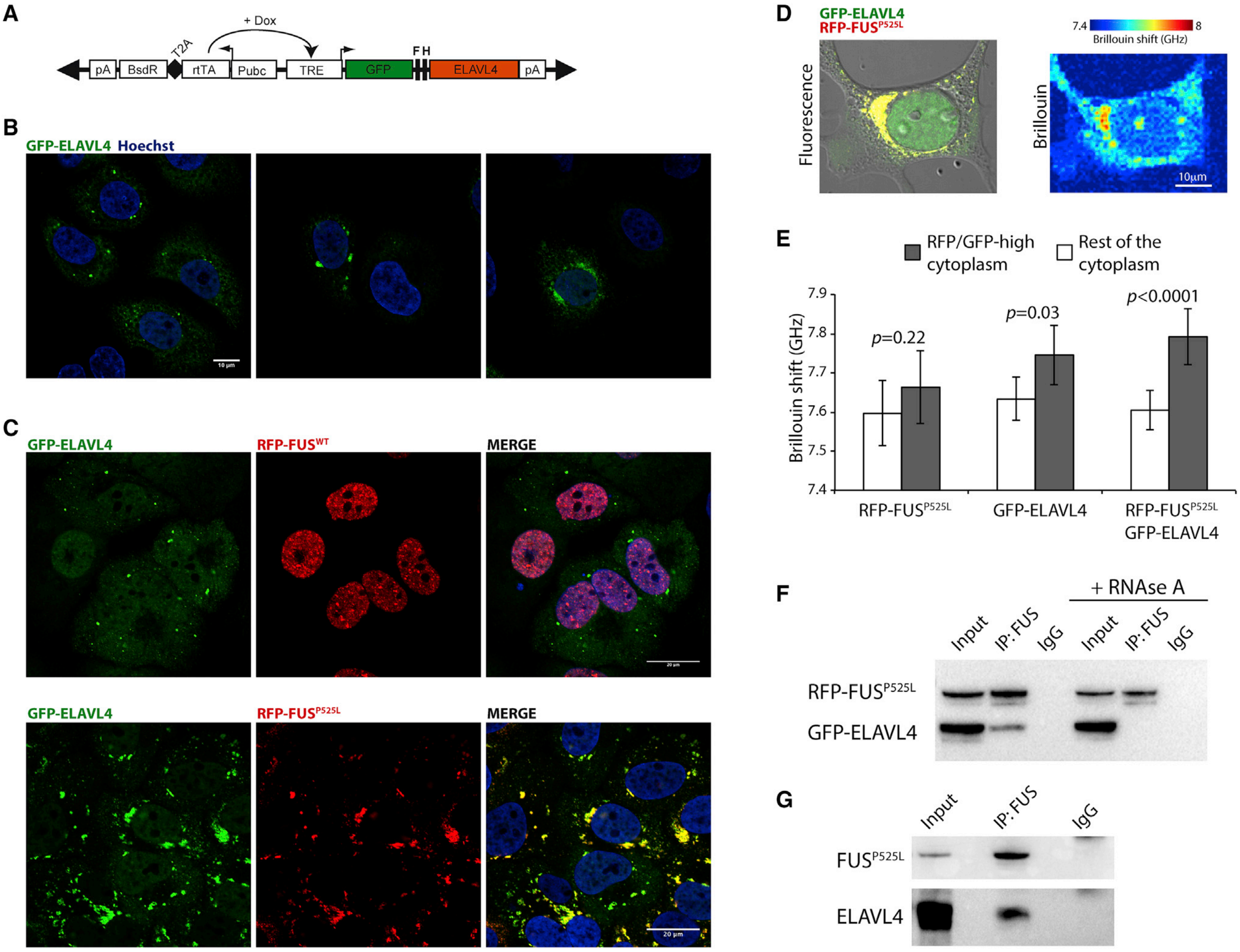

Figure 3. ELAVL4 Forms Cytoplasmic Speckles and Interacts with FUS^{P525L} in the Cytoplasm

(A) Schematic representation of the enhanced piggyBac transposable vector for doxycycline conditional expression of GFP-ELAVL4 (epB-Bsd-TT-GFP-ELAVL4). F, FLAG tag; H, HA tag; pA, polyadenylation signal; BsdR, blasticidin resistance gene; T2A, self-cleavage peptide; rtTA, TET transactivator protein gene; Pubc, human ubiquitin C constitutive promoter; TRE, TET responsive element; Dox, doxycycline. Triangles represent terminal repeats of the transposon.

(B) Confocal images of HeLa cells stably transduced with the epB-Bsd-TT-GFP-ELAVL4 vector and induced with doxycycline for 24 h. Hoechst (blue) marks nuclei. Scale bar, 10 µm.

(C) Confocal images of HeLa cells stably transduced with the epB-Bsd-TT-GFP-ELAVL4 and epB-Puro-TT-RFP-FUS^{WT} (top panels) or epB-Puro-TT-RFP-FUS^{P525L} (bottom panels) vectors and induced with doxycycline for 24 h. In the MERGE panels DAPI (blue) marks nuclei. Scale bar, 20 µm.

(D) Representative images acquired with the confocal microscope (left) and with the BDB microscope (right) of a HeLa cell expressing GFP-ELAVL4 and RFP-FUS^{P525L}. Scale bar, 10 µm.

(E) Bar plot of the Brillouin frequency shift in cytoplasmic compartments of HeLa cells expressing GFP-ELAVL4, RFP-FUS^{P525L}, or both. Grey bars are relative to regions of the cytoplasm with high RFP and/or GFP signal. White bars refer to the rest of the cytoplasm. Histogram bars represent the average (6, 5, and 12 cells, respectively; two independent experiments) and error bars indicate the SD (p values from Student's t test; paired; two tails).

(F) Co-immunoprecipitation of RFP-FUS^{P525L} and GFP-ELAVL4 from cytoplasmic extracts of HeLa cells treated as in (C). Immunoprecipitation was performed using an anti-FUS antibody. Samples were untreated or treated with RNaseA before immunoprecipitation. RFP-FUS^{P525L} and GFP-ELAVL4 bands were revealed with an anti-FLAG antibody.

(G) Co-immunoprecipitation of endogenous FUS^{P525L} and ELAVL4 in cytoplasmic extract of motor neuron by using a FUS antibody and revealed by western blot with anti-FUS and anti-ELAVL4 antibodies.

See also Figure S4.

expressing GFP-ELAVL4 and RFP-FUS^{P525L}, each alone or in combination, were imaged first with the confocal microscope to localize the fluorescence signals and then with the BDB microscope. Representative images are shown in Figure 3D and Figures S4D and S4E. The Brillouin frequency shift values associated to the real part of the longitudinal bulk modulus M' (Prevedel et al., 2019) were comparatively measured in cytoplasmic regions where GFP and/or RFP signal was more concentrated (i.e., bright

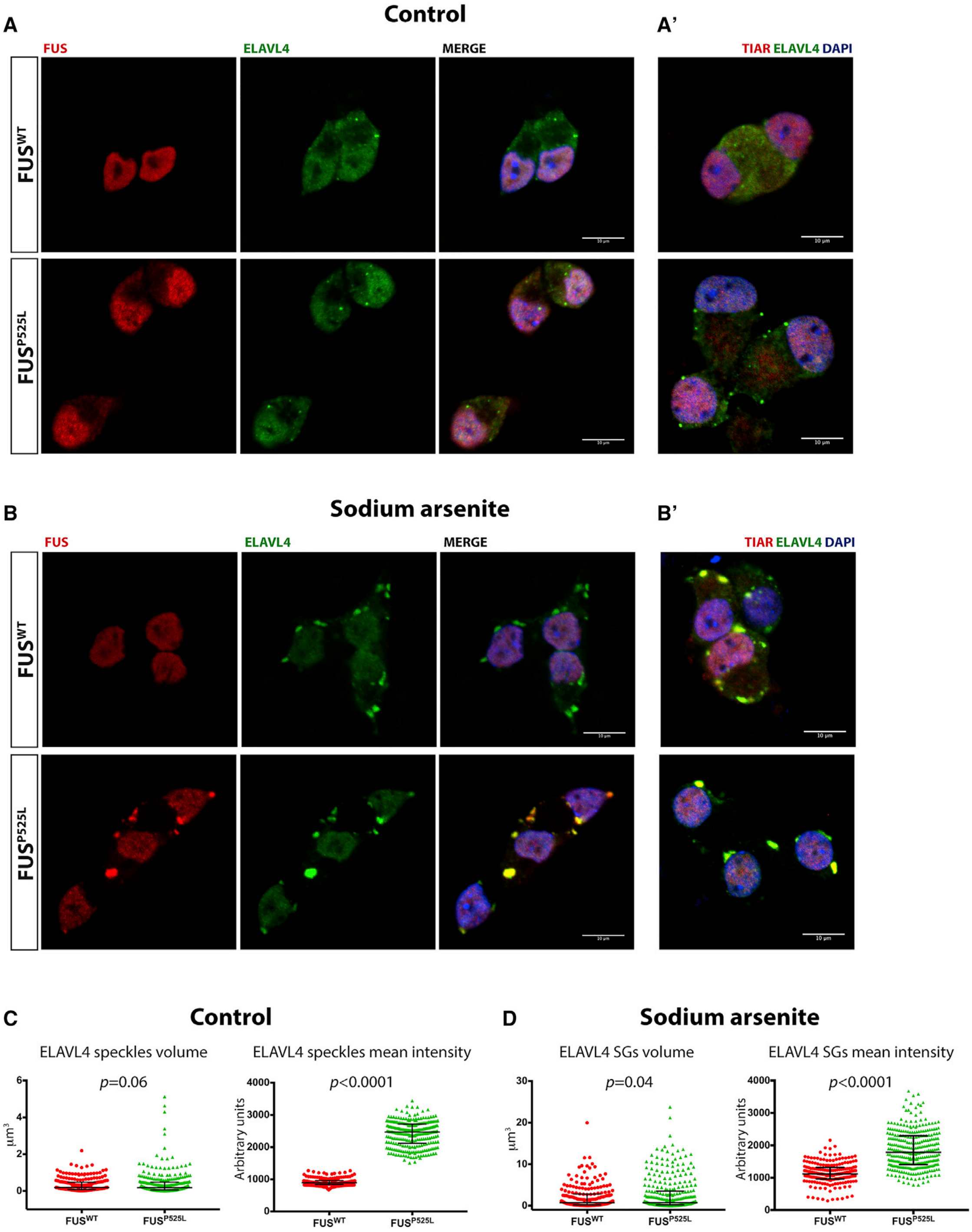

Figure 4. ELAVL4 and FUS Localization in Human iPSC-Derived Motor Neurons in Normal or Stress Conditions

(A) Immunostaining for FUS (red) and ELAVL4 (green) in FUS^{WT} and $\text{FUS}^{\text{P525L}}$ MNs at 7 days after FACS purification in untreated control conditions. In the MERGE panels, DAPI (blue) stains nuclei.

(A') Immunostaining for ELAVL4 (green), TIAR (red), and with DAPI (blue) in cells treated as in (A). Single channels are shown in Figure S6.

(B) Immunostaining for FUS (red) and ELAVL4 (green) in FUS^{WT} and $\text{FUS}^{\text{P525L}}$ MNs at 7 days after FACS purification, cultured in presence of 0.5 mM sodium arsenite for 90 min. In the MERGE panels, DAPI (blue) stains nuclei.

(B') Immunostaining for ELAVL4 (green), TIAR (red), and with DAPI (blue) in cells treated as in (B). Single channels are shown in Figure S6. Scale bar, 10 µm.

(legend continued on next page)

granules or perinuclear regions in the case of single protein expression and double-positive speckles for double transgenic cells; gray bars in Figure 3E) and in the rest of the cytoplasm (white bars in Figure 3E). In HeLa cells expressing single proteins, the difference in the Brillouin frequency shift was not significant for RFP-FUS^{P525L} and was significant for GFP-ELAVL4. Notably, this difference was more consistent and highly significant in cells expressing both GFP-ELAVL4 and RFP-FUS^{P525L}. This result suggests that double-positive speckles represent stiff cytoplasmic structures showing different viscoelastic characteristics from the rest of the cytoplasm.

Co-localization of mutant FUS and ELAVL4 in the cytoplasm suggested the possibility of a direct interaction between the two proteins. To verify this hypothesis, we performed co-immunoprecipitation (coIP) in cytoplasmic extracts of double reporter HeLa cells. ELAVL4 was co-immunoprecipitated with mutant FUS, and this interaction was RNA-dependent, as the ELAVL4 signal was absent in extracts treated with RNase A (Figure 3F; Figure S4F). Furthermore, interaction between endogenous FUS^{P525L} and ELAVL4 proteins, untagged and expressed at physiological levels, was detected in human iPSC-derived MNs (Figure 3G).

Collectively, these data show that ectopic expression of ELAVL4 and mutant FUS results in their co-localization in cytoplasmic speckles, which do not represent SGs and display different biomechanical properties from the rest of the cytoplasm. Moreover, mutant FUS interacts with ELAVL4 in the cytoplasm of human iPSC-derived MNs.

FUS^{P525L} and ELAVL4 Localization in iPSC-Derived MNs

The *ELAVL4* gene is a member of the neural ELAVL (nELAVL) family, whose expression pattern has been extensively characterized, temporally and spatially, in mouse and rat (reviewed in Bronicki and Jasmin, 2013). Rodent *Elavl4* mRNA expression was detected early during embryonic brain development and attenuated postnatally. In the adult nervous system its expression is mostly restricted to specific neuronal populations. In the rat spinal cord, *Elavl4* mRNA levels were found to be highest within the ventral MNs as compared to the dorsal sensory neurons (Clayton et al., 1998). We took advantage of the Genotype-Tissue Expression (GTEx) portal to identify the *ELAVL4* expression pattern in human. This survey suggested that human *ELAVL4* transcripts are mainly restricted to the central nervous system and mostly absent in other tissues (Figure S5A). In our previous work, we have analyzed the transcriptome of differentiated FUS^{WT} iPSCs sorted according to the expression of a MN reporter construct, consisting of the GFP coding sequence under the control of the Hb9 promoter (De Santis et al., 2017). We used this dataset to assess the expression of nELAVL factors in iPSC-derived cell populations representative of the ventral spinal cord. *ELAVL4* and *ELAVL2* were enriched in the Hb9::GFP-positive MN population, whereas *ELAVL3*, *ELAVL1* (*HuR*), and *FUS* did not show significant differences in the two samples (Figure S5B). Differential expression of *ELAVL4* was confirmed in the Hb9::GFP-positive MN populations at the transcript (Figure S5C) and protein (Figure S5D) levels. Moreover, immunostaining analysis performed on the unsorted mixed population of iPSC-derived cells showed ELAVL4 expression in the TUJ1-positive fraction (Figure S5E), mostly represented by ISL1/2-positive MNs (Figure S5F; De Santis et al., 2017). Taken together, the GTEx interrogation and the expression analysis in iPSC-derived cells suggest that human *ELAVL4* is a neural gene expressed in spinal MNs.

We next characterized ELAVL4 intracellular localization in MNs, in the presence of wild-type or mutant FUS. Pure populations of FUS^{WT} and FUS^{P525L} iPSC-derived MNs were stained with antibodies for FUS and ELAVL4 and analyzed at the confocal microscope. In normal culture conditions, ELAVL4 localized in both nuclear and cytoplasmic compartments and mutant FUS did not change this pattern (Figure 4A). Cytoplasmic ELAVL4-positive speckles, reminiscent of those formed upon ectopic expression in HeLa, could be observed in MNs as well. However, cytoplasmic FUS was not confined in these ELAVL4 speckles in mutant MNs. In normal conditions, ELAVL4 speckles do not co-localize with the SG marker TIAR (Figure 4A'; Figure S6A). We then evaluated FUS and ELAVL4 localization upon sodium arsenite (ARS) treatment, which induces oxidative stress and SG formation. In ARS-treated FUS^{WT} MNs, ELAVL4 re-localized into cytoplasmic SGs, displaying a bigger size than ELAVL4-positive speckles observed in unstressed cells (Figure 4B; Figure S6B). Wild-type FUS maintained its nuclear localization, as expected. In stressed FUS^{P525L} MNs we observed the formation of SGs that were both FUS- and ELAVL4-positive (Figures 4B and 4B'). Quantitative analysis of the volumes and ELAVL4 mean signal intensity within the speckles revealed that although their size is not altered by the FUS mutation, ELAVL4 levels are significantly increased in the speckles formed in FUS^{P525L} MNs (Figure 4C). The same analysis on cells stressed with ARS showed that in mutant MNs the SGs contain a higher amount of ELAVL4 protein (Figure 4D). These findings were confirmed in MNs generated from an independent pair of isogenic FUS^{WT} and FUS^{P525L} iPSCs (Figures S6C and S6D). We next explored the possibility that mutant FUS and ELAVL4 share some mRNA target in the MN. The interactome of nELAVLs in human brain has been recently reported (Scheckel et al., 2016). In this dataset, 95.5% of the reads were mapped in introns and 3′ UTRs. To identify candidates that might mediate the interaction of ELAVL4 and FUS^{P525L} in the cytoplasm, we crossed the 3′ UTR nELAVLs targets with our PAR-CLIP datasets. As shown in Figure S7A, several mRNA are bound by both nELAVLs and FUS. Interestingly, nELAVLs share a higher number of common targets with

---

(C) Scatter dot plot representing the quantitative analysis, in one representative experiment, of the volumes (left) and mean intensity (total signal intensity normalized for the volume) of ELAVL4 signal (right) of the ELAVL4-positive speckles in FUS^{WT} (n = 23) and FUS^{P525L} (n = 38) MNs as shown in (A).

(D) Scatter dot plot representing the quantitative analysis of the volumes (left) and mean intensity (total signal intensity normalized for the volume), in one representative experiment, of ELAVL4 signal (right) of the ELAVL4-positive SGs in FUS^{WT} (n = 23) and FUS^{P525L} (n = 30) MNs as shown in (B). In all graphs the bars indicate the median with interquartile range. p values from Student's t test (unpaired; two tails) are indicated.

See also Figures S5, S6, and S7.

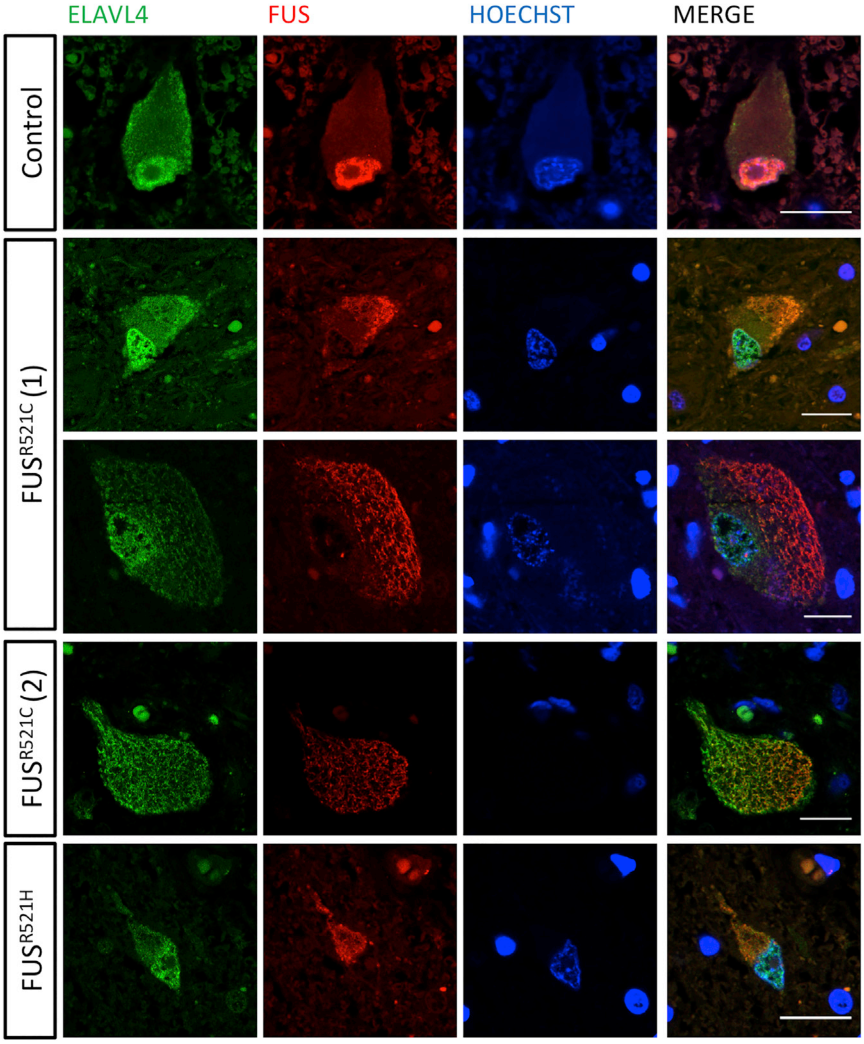

Figure 5. ELAVL4 Immunostaining Analysis in FUS Patients' Specimens

Immunofluorescence showing spinal cord motor neurons of ALS patients harboring the indicated FUS mutations and control. Sections were stained with anti-FUS (red) and anti-ELAVL4 (green) antibodies and counterstained with Hoechst. Scale bar, 20 μm. Characteristics of patients and controls are reported in Table S2.

FUS^{P525L} compared to FUS^{WT}. This result was further confirmed by overlapping our PAR-CLIP results with the interactome of ELAVL4 in murine NSC-34 MN-like cells (Tebaldi et al., 2018). Notably, the top 30 previously identified ELAVL4 targets are all bound by FUS^{P525L} in their 3′ UTR (Figure S7B). Thus, a common set of target transcripts might contribute, at least partially, to the co-recruitment of FUS^{P525L} and ELAVL4 in cytoplasmic granules of MNs.

These findings showed that ELAVL4 is a component of SGs formed upon oxidative stress in human MNs and that ELAVL4 and FUS co-localize in these compartments only in FUS mutant cells. Moreover, both ELAVL4 speckles (in normal conditions) and SGs (upon oxidative stress) contain increased levels of ELAVL4 in FUS mutant MNs.

ELAVL4 Is a Component of Pathological Inclusions in ALS Patients' Specimens

We have previously shown the detection of ELAVL4 in mutant FUS inclusions in spinal MNs from an ALS patient carrying the R521C mutation (Blokhuis et al., 2016). To assess whether such co-localization generally occurs in FUS ALS patients, we performed immunohistochemistry for FUS and ELAVL4 on spinal cord sections from two additional patients harboring the R521C mutation and one patient with the R521H mutation. In agreement with the observation that late-onset cases, such as those with mutations in the R521 residue, mostly display tangle-like neuronal cytoplasmic inclusions (Mackenzie et al., 2011), in patients' specimens we detected FUS-positive thick filaments within the perikaryon, either with a globose arrangement or with a flame-shaped appearance extending into the proximal axon (Figure 5). FUS depletion from the nucleus was also evident. Notably, even though the nuclear fraction of ELAVL4 appeared maintained, ELAVL4 showed altered localization in the cytoplasm of patients' MNs, with fibrillar appearance and co-localization with FUS-positive filaments. We then extended this analysis to sporadic ALS patients, devoid of mutations in known ALS genes, and in ALS patients carrying the pathological C9ORF72 expansion. In sporadic patients' specimens phosphorylated TDP-43 (pTDP-43)-positive pathological cytoplasmic inclusions, a highly consistent feature in sporadic and familial forms of TDP-43 proteinopathies (Neumann et al., 2009), also showed localization of ELAVL4 (Figure 6; Figure S8). In C9ORF72 patients, we detected fewer pTDP-43-positive neurons and less evident co-localization of pTDP-43 and ELAVL4 in pathological inclusions (Figure S8).

These findings point to ELAVL4 as a common component of FUS-positive and pTDP-43-positive neuronal cytoplasmic inclusions, in FUS and sporadic ALS patients, respectively.

DISCUSSION

RNA metabolism alterations have been shown to play a fundamental role in ALS. Single ALS mutations in RBPs have been proposed to be disease-causative, but the underlying mechanisms remain poorly understood. Interestingly, individual RBPs act often in concert with other RBPs in complex regulatory networks, comprised of feedback loops and cross-regulation.

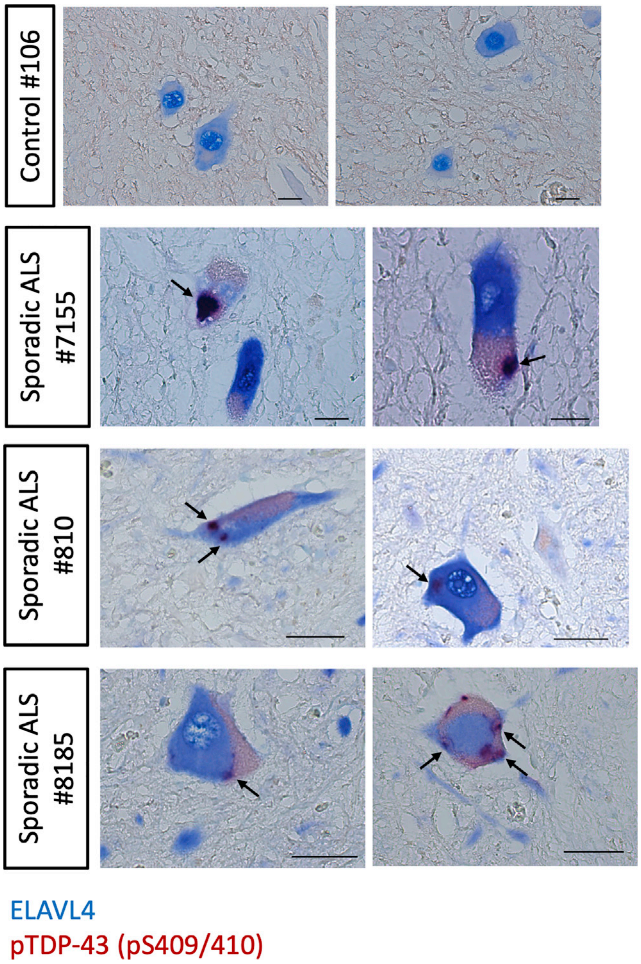

Figure 6. ELAVL4 Immunohistochemistry Analysis in Sporadic ALS Patients' Specimens

Immunohistochemistry on spinal cord samples from sporadic ALS patients. For double immunohistochemistry, sections were labeled with anti-ELAVL4 (blue) and anti-pTDP-43 (pS409/410) (red). Scale bar: 20 μm. Arrows indicate pTDP-43 and ELAVL4 double positive cytoplasmic inclusions. Characteristics of patients and controls are reported in Table S3. See also Figure S8.

The significance of the crosstalk between ALS-linked RBPs and other factors involved in RNA metabolism deserves deeper investigation.

ALS-linked mutations in FUS may alter other RBPs levels by at least four mechanisms: (1) dysregulation of alternative splicing (Nakaya et al., 2013; Zhou et al., 2013); (2) stalling RNA polymerase II and prematurely terminating transcription (Masuda et al., 2015); (3) impairment of the production of targeting miRNAs (Morlando et al., 2012; Dini-Modigliani et al., 2014; Emde et al., 2015; De Santis et al., 2017); and (4) increasing translation and/or stability by aberrant binding to the 3′ UTR in the cytoplasm (present study). The first three mechanisms are consistent with a loss-of-function effect of the mutation, which would reduce the nuclear fraction of FUS and indeed can be mimicked by FUS downregulation. Aberrant 3′ UTR binding would instead represent the gain of a toxic function for mutant FUS, due to its mis-localization in the cytoplasm. The PAR-CLIP analysis suggests that mutant FUS proteins have a larger number of targets than the wild type. As ALS mutations are not expected to alter FUS affinity for RNA (Bentmann et al., 2012; Daigle et al., 2013), we speculate that this could be primarily due to different sub-cellular localization of the mutated protein. Although previous work showed that FUS knock down resulted in decreased mRNA stability (Udagawa et al., 2015; Kapeli et al., 2016; Yokoi et al., 2017), we propose here that ALS mutant FUS binding to the 3′ UTR of *ELAVL4*, and possibly other genes, has an opposite outcome resulting in an increase of target protein production in MNs. Together with our previous findings, our results suggest a double mechanism by which ELAVL4 levels could be increased in mutant FUS MNs: an indirect effect of the mutation would be mediated by the decrease of miR-375 levels (De Santis et al., 2017) and a direct outcome would result by 3′ UTR binding in the cytoplasm. Mechanistic insights into the regulation of ELAVL4 and other RBPs by FUS might lead to a better understanding of the basis of RNA metabolism dysregulation in ALS.

At the protein level, direct interaction of wild-type FUS and ELAVL4 in neural cells has been previously reported (Groen et al., 2013; Udagawa et al., 2015; Blokhuis et al., 2016; Yokoi et al., 2017). In mouse hippocampal neurons, both FUS and ELAVL4 proteins bind the 3′ UTR of SynGAP, a factor involved in spine maturation (Yokoi et al., 2017). Knock down of either FUS or ELAVL4 resulted in the interaction of SynGAP 3′ UTR with ELAVL1, leading to destabilization of the transcript. Thus, FUS and ELAVL4 cooperatively increase mRNA stability by 3′ UTR binding. A similar mechanism may promote the production of GluA1, an AMPA receptor subunit (Udagawa et al., 2015; Yokoi et al., 2017). These studies proposed that the interplay between wild-type FUS and ELAVL4 is crucial for synaptic morphology and cognitive functions in the context of frontotemporal lobar degeneration (FTLD). In the present study, we showed that mutant FUS and ELAVL4 interact at the protein level in the cytoplasm of MNs. This would represent an aberrant interaction occurring in mutant cells only, where nuclear import of the mutated FUS protein is impaired. We show that interaction between the two proteins occurs in a RNA-dependent manner, and this observation has two possible explanations. One possibility is that ELAVL4 and FUS^{P525L} need a RNA bridge to interact. To this regard, crossing our dataset with previous studies on the interactome of neural ELAV proteins suggested that the two RBPs share a common set of targets. However, it has been previously reported that RNA binding changes FUS conformation and activity (Wang et al., 2008), possibly affecting protein interactors in coIP experiments. Thus, we cannot exclude direct protein-protein binding. Under stress conditions, both mutant FUS and ELAVL4 get recruited into SGs. The consequences of their interaction and re-localization, also in light of the fact that ELAVL4 levels would be aberrantly increased in mutant MNs, could be relevant for ALS pathology. We propose a model, depicted in Figure 7A. In normal MNs, FUS is mostly nuclear and ELAVL4 levels are controlled by miR-375. In young mutant MNs, FUS is partially de-localized in the cytoplasm, where it binds *ELAVL4* 3′ UTR. Nuclear FUS reduction would also result in a decrease of miR-375. As a consequence, ELAVL4 protein levels start to increase. This situation is mimicked in our

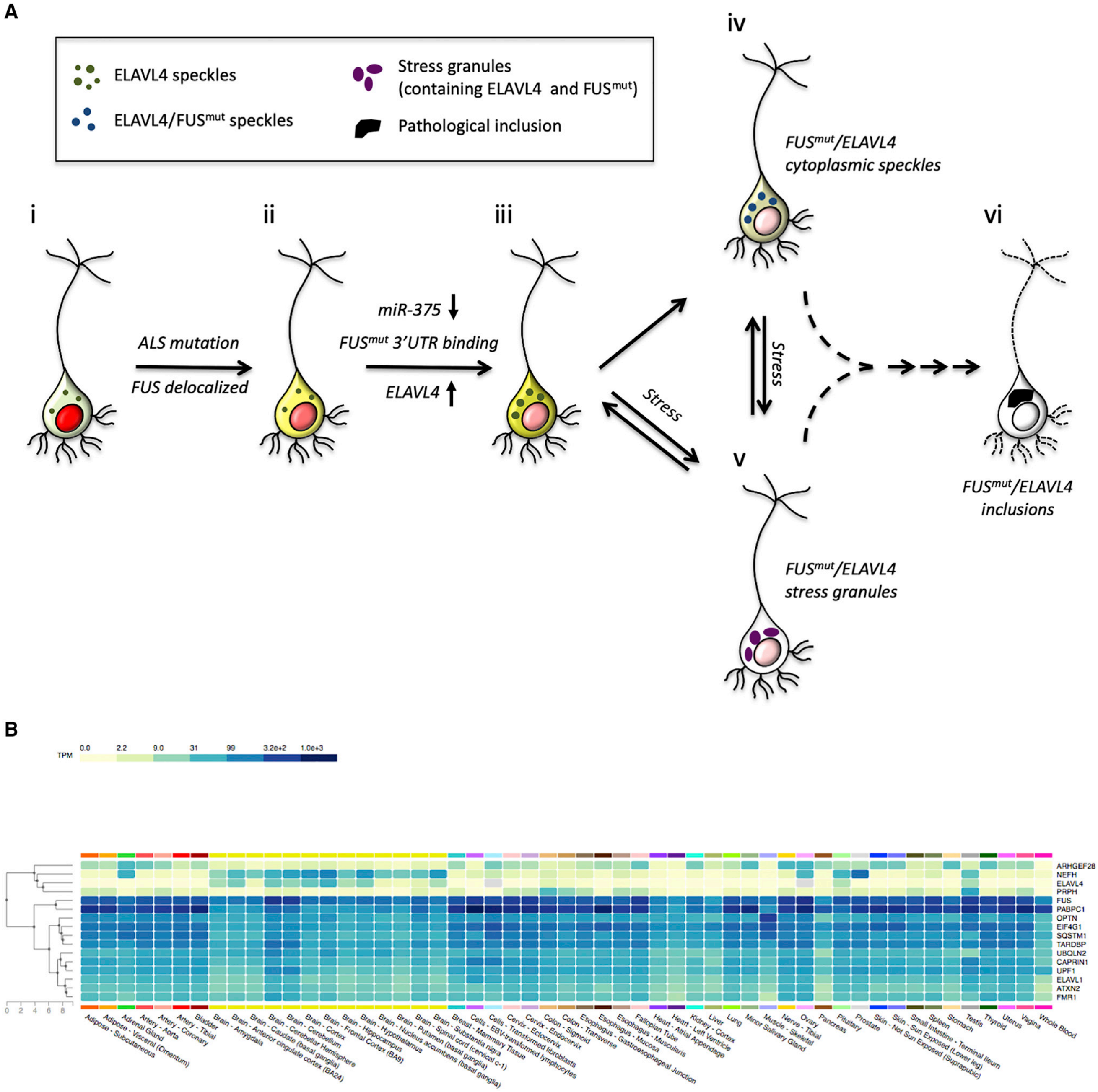

Figure 7. Model and Expression of FUS Pathological Inclusion Components in Human

(A) Model of the aberrant crosstalk between mutant FUS and ELAVL4 in ALS. (i) In normal conditions FUS (red) is mainly localized in the nucleus. ELAVL4 (green) is localized both in the nucleus and in the cytoplasm, where it has a diffuse localization punctuated by speckles. Human iPSC-derived FUS^{WT} MNs would be representative of this situation. (ii) ALS mutations in the nuclear localization signal cause FUS partial de-localization in the cytoplasm. Mutant FUS binds *ELAVL4* 3′UTR. Moreover, as a consequence of FUS nuclear depletion, miR-375 levels decrease. These events gradually cause an increase of ELAVL4 protein levels. Human iPSC-derived FUS^{P525L} MNs would be representative of this situation. (iii) Over time, ELAVL4 protein levels are increasingly augmented, forming bigger speckles in the cytoplasm. It is possible that protein-protein interaction with ELAVL4 results in further mutant FUS accumulation in the cytoplasm. This, in turn, would further increase ELAVL4 levels by the above-mentioned mechanisms. (iv) Increased levels of both ELAVL4 and mutant FUS in the cytoplasm and their interaction might lead to the formation of speckles containing both proteins, independently from cellular stress. This situation cannot be observed in human iPSC-derived MNs, which correspond to "young" MNs. However, mutant FUS/ELAVL4 speckles are formed in the cytoplasm of HeLa cells overexpressing both proteins. (v) In presence of cellular stress, e.g., oxidative stress, cytoplasmic mutant FUS and ELAVL4 proteins co-localize in stress granules. We observe this phenomenon in both transgenic HeLa cells and human iPSC-derived MNs. (vi) Alteration of granules/speckles biomechanical properties due to mutant FUS and/or increased ELAVL4 would lead over time to the formation of ALS pathological inclusions, in which mutant FUS, ELAVL4, and SG markers can be detected.

(legend continued on next page)

iPSC-derived MN model system, in which we observed an increased amount of ELAVL4 in the speckles. Over time, mutant FUS would be increasingly accumulated in the cytoplasm, paralleled by an increment of ELAVL4 levels. We hypothesize that over a given threshold, mutant FUS and ELAVL4 co-localize in cytoplasmic speckles. Although iPSC-derived MNs, which correspond to a fetal stage (Sances et al., 2016), could not recapitulate this “aged” condition, we observed double-positive speckles in HeLa cells co-expressing mutant FUS and ELAVL4 beyond physiological levels. When analyzed with the BDB microscope, these speckles showed a significant increase of the Brillouin frequency shift compared to the rest of the cytoplasm. As this parameter can provide information about the condensation state of the material analyzed (Antonacci et al., 2018), the onset of a liquid-to-solid phase transition occurring in the speckles might be inferred from this analysis. These structures might, therefore, represent the precursors of the pathological inclusions or aggregates found in patients’ MNs. This hypothesis is supported by evidences from the current work and by our previous report (Blokhuis et al., 2016), showing FUS/ELAVL4 colocalization in cytoplasmic aggregates in the spinal cord of FUS ALS patients. Pathological inclusions have been shown to contain SG markers (Dormann et al., 2010). We observed co-localization of mutant FUS and ELAVL4 in SGs in iPSC-derived MNs under oxidative stress conditions. Consistent with the increased levels of ELAVL4 in these cells, SGs formed in FUS^{P525L} MNs contain a higher amount of ELAVL4. It is possible that, over time, transient SGs coalesce with mutant FUS/ELAVL4 speckles, contributing to pathological inclusion formation. Notably, among a number of components of FUS-positive pathological inclusions detected so far in ALS patients, only NFH had been identified as a neural-enriched factor. In the GTEx dataset, all other factors and FUS itself are reported as ubiquitously expressed in all tissues analyzed (Figure 7B; Figure S9). This includes other RBPs and SG components, such as PABP, eIF4G, CAPRIN1, and FMRP. On the contrary, ELAVL4 is a neural-specific RBP associated with the pathological inclusions of FUS patients. This evidence, together with the BDB analysis, lead to the speculation that the FUS/ELAVL4 interaction could alter the biomechanical properties of these structures in neural cells only. Importantly, localization of ELAVL4 in pathological cytoplasmic inclusions occurs also in non-FUS sporadic ALS. As the direct interaction between ELAVL4 and TDP-43 has been previously described in mouse MNs (Fallini et al., 2012), we might speculate that in these patients recruitment of ELAVL4 in pTDP-43-positive inclusions occurs by an aberrant crosstalk with TDP-43.

In conclusion, this study reports a comprehensive analysis of wild-type and mutant FUS RNA interactome in the cell type primarily affected by ALS, i.e., the human MN. Among selective mutant FUS targets, we identified several RBPs, including ELAVL4, which represents a neural-specific component of SGs and ALS pathological inclusions in both FUS patients and in sporadic ALS with pTDP-43 proteinopathy. We, therefore, propose ELAVL4 as a RBP with a potential role in ALS pathogenesis.

STAR★METHODS

Detailed methods are provided in the online version of this paper and include the following:

- KEY RESOURCES TABLE
- CONTACT FOR REAGENT AND RESOURCE SHARING
- EXPERIMENTAL MODEL AND SUBJECT DETAILS
  - ○ Human iPSC lines
  - ○ HeLa cells
  - ○ Spinal cord samples from ALS patients
- METHOD DETAILS
  - ○ PAR-CLIP analysis
  - ○ Plasmid construction and transfection
  - ○ Luciferase assay
  - ○ Co-immunoprecipitation
  - ○ Immunostaining
  - ○ Image acquisition, deconvolution and analysis
  - ○ Immunohistochemistry
  - ○ BDB microscopy
  - ○ Gene expression analysis
- QUANTIFICATION AND STATISTICAL ANALYSIS
- DATA AVAILABILITY

SUPPLEMENTAL INFORMATION

Supplemental Information can be found online at https://doi.org/10.1016/j.celrep.2019.05.085.

ACKNOWLEDGMENTS

The authors wish to thank the Imaging Facility and the Flow Cytometry Facility at Center for Life Nano Science, Istituto Italiano di Tecnologia, for support and technical advice. We thank Dr. Giulia M.R. De Luca (Scientific Volume Imaging, BV) for helpful discussion on deconvolution with the Huygens software. This work was partially supported by AriSLA pilot grant 2016 “StressFUS” to A.R.; ERC-2013 (AdG 340172–MUNCODD), AriSLA full grant 2014 “ARCI,” Human Frontiers Science Program Award RGP0009/2014, and Epigen-Epigenomics Flagship Project and Telethon (GGP16213) to I.B.; ALS Stichting grants TOTALS and FUNCTIONALS, Prinses Beatrix Spierfonds W.OR15-17 to R.J.P.; and ALS Stichting grant “The Dutch ALS Tissue Bank” to E.A. We acknowledge the team who helped in the collection of ALS tissue samples (Prof. Dr. D. Troost, Prof. Dr. M. de Visser, Dr. A.J. van der Kooi, and Dr. J. Raaphorst).

AUTHOR CONTRIBUTIONS

A.R., R.D.S., and V.A. conceived the project, designed the work, and analyzed the results. R.D.S. performed the PAR-CLIP, the reporter assays and the coIP, and contributed to the bioinformatics analysis and paper writing. V.A. cultured

---

As previously proposed (Bentmann et al., 2013), three modes of pathological inclusions formation are possible: SG-dependent, aggregation-dependent, aggregation- and SG-dependent.

(B) Heatmap representing gene expression levels in different human tissues from the GTEx Portal (https://www.gtexportal.org/home/). Genes that are known components of FUS pathological inclusions (Blokhuis et al., 2013, 2016) are reported. The ubiquitous ELAVL family member *ELAVL1* (*HuR*) is also shown. Expression values are shown in TPM (transcripts per million), calculated from a gene model with isoforms collapsed to a single gene. See also Figure S9.

and differentiated MNs, quantified ELAVL4 levels in MNs, performed the stainings, and contributed to paper writing. V.d.T. acquired and analyzed microscopy images and performed quantitative analysis of ELAVL4 from confocal images. A.C. performed the bioinformatics analysis of the PAR-CLIP. L.S. contributed to cell culture and MN differentiation and to the PAR-CLIP. M.G.G. contributed to the generation of plasmids, cell culture, and MN differentiation. G.A. performed BDB acquisition and analysis. G.P. performed MNs sorting. J.J.A. and E.A. provided patients' tissues and immunohistochemistry on sporadic and FUS ALS patients' samples. E.S.-L. and R.J.P. contributed to the staining on FUS patients' samples. E.W. contributed to PAR-CLIP and bioinformatics analysis. M.L. coordinated the PAR-CLIP work. I.B. provided critical feedback and helped shape the research. A.R. coordinated the work and wrote the paper.

DECLARATION OF INTERESTS

The authors declare no competing interests.

Received: September 18, 2018
Revised: April 4, 2019
Accepted: May 22, 2019
Published: June 25, 2019

REFERENCES

Aken, B.L., Achuthan, P., Akanni, W., Amode, M.R., Bernsdorff, F., Bhai, J., Billis, K., Carvalho-Silva, D., Cummins, C., Clapham, P., et al. (2017). Ensembl 2017. Nucleic Acids Res. *45*, D635–D642.

Anderson, P., and Kedersha, N. (2009). RNA granules: post-transcriptional and epigenetic modulators of gene expression. Nat. Rev. Mol. Cell Biol. *10*, 430–436.

Antonacci, G., and Braakman, S. (2016). Biomechanics of subcellular structures by non-invasive Brillouin microscopy. Sci. Rep. *6*, 37217.

Antonacci, G., de Turris, V., Rosa, A., and Ruocco, G. (2018). Background-deflection Brillouin microscopy reveals altered biomechanics of intracellular stress granules by ALS protein FUS. Commun Biol *1*, 139.

Benhalevy, D., McFarland, H.L., Sarshad, A.A., and Hafner, M. (2017). PAR-CLIP and streamlined small RNA cDNA library preparation protocol for the identification of RNA binding protein target sites. Methods *118–119*, 41–49.

Bentmann, E., Neumann, M., Tahirovic, S., Rodde, R., Dormann, D., and Haass, C. (2012). Requirements for stress granule recruitment of fused in sarcoma (FUS) and TAR DNA-binding protein of 43 kDa (TDP-43). J. Biol. Chem. *287*, 23079–23094.

Bentmann, E., Haass, C., and Dormann, D. (2013). Stress granules in neurodegeneration–lessons learnt from TAR DNA binding protein of 43 kDa and fused in sarcoma. FEBS J. *280*, 4348–4370.

Blokhuis, A.M., Groen, E.J.N., Koppers, M., van den Berg, L.H., and Pasterkamp, R.J. (2013). Protein aggregation in amyotrophic lateral sclerosis. Acta. Neuropathol. *125*, 777–794.

Blokhuis, A.M., Koppers, M., Groen, E.J., van den Heuvel, D.M., Dini Modigliani, S., Anink, J.J., Fumoto, K., van Diggelen, F., Snelting, A., Sodaar, P., et al. (2016). Comparative interactomics analysis of different ALS-associated proteins identifies converging molecular pathways. Acta. Neuropathol. *132*, 175–196.

Bronicki, L.M., and Jasmin, B.J. (2013). Emerging complexity of the HuD/ELAVl4 gene; implications for neuronal development, function, and dysfunction. RNA *19*, 1019–1037.

Clayton, G.H., Perez, G.M., Smith, R.L., and Owens, G.C. (1998). Expression of mRNA for the elav-like neural-specific RNA binding protein, HuD, during nervous system development. Brain Res. Dev. Brain Res. *109*, 271–280.

Colombrita, C., Onesto, E., Megiorni, F., Pizzuti, A., Baralle, F.E., Buratti, E., Silani, V., and Ratti, A. (2012). TDP-43 and FUS RNA-binding proteins bind distinct sets of cytoplasmic messenger RNAs and differently regulate their post-transcriptional fate in motoneuron-like cells. J. Biol. Chem. *287*, 15635–15647.

Courchaine, E.M., Lu, A., and Neugebauer, K.M. (2016). Droplet organelles? EMBO J. *35*, 1603–1612.

D'Andrea, D., Grassi, L., Mazzapioda, M., and Tramontano, A. (2013). FIDEA: a server for the functional interpretation of differential expression analysis. Nucleic Acids Res. *41*, W84–W88.

Daigle, J.G., Lanson, N.A., Jr., Smith, R.B., Casci, I., Maltare, A., Monaghan, J., Nichols, C.D., Kryndushkin, D., Shewmaker, F., and Pandey, U.B. (2013). RNA-binding ability of FUS regulates neurodegeneration, cytoplasmic mislocalization and incorporation into stress granules associated with FUS carrying ALS-linked mutations. Hum. Mol. Genet. *22*, 1193–1205.

De Santis, R., Santini, L., Colantoni, A., Peruzzi, G., de Turris, V., Alfano, V., Bozzoni, I., and Rosa, A. (2017). FUS Mutant Human Motoneurons Display Altered Transcriptome and microRNA Pathways with Implications for ALS Pathogenesis. Stem Cell Reports *9*, 1450–1462.

Deng, H., Gao, K., and Jankovic, J. (2014). The role of FUS gene variants in neurodegenerative diseases. Nat. Rev. Neurol. *10*, 337–348.

Dini Modigliani, S., Morlando, M., Errichelli, L., Sabatelli, M., and Bozzoni, I. (2014). An ALS-associated mutation in the FUS 3′-UTR disrupts a microRNA-FUS regulatory circuitry. Nat. Commun. *5*, 4335.

Dormann, D., and Haass, C. (2011). TDP-43 and FUS: a nuclear affair. Trends Neurosci. *34*, 339–348.

Dormann, D., Rodde, R., Edbauer, D., Bentmann, E., Fischer, I., Hruscha, A., Than, M.E., Mackenzie, I.R.A., Capell, A., Schmid, B., et al. (2010). ALS-associated fused in sarcoma (FUS) mutations disrupt Transportin-mediated nuclear import. EMBO J. *29*, 2841–2857.

Emde, A., Eitan, C., Liou, L.-L., Libby, R.T., Rivkin, N., Magen, I., Reichenstein, I., Oppenheim, H., Eilam, R., Silvestroni, A., et al. (2015). Dysregulated miRNA biogenesis downstream of cellular stress and ALS-causing mutations: a new mechanism for ALS. EMBO J. *34*, 2633–2651.

Fallini, C., Bassell, G.J., and Rossoll, W. (2012). The ALS disease protein TDP-43 is actively transported in motor neuron axons and regulates axon outgrowth. Hum. Mol. Genet. *21*, 3703–3718.

Fujii, R., Okabe, S., Urushido, T., Inoue, K., Yoshimura, A., Tachibana, T., Nishikawa, T., Hicks, G.G., and Takumi, T. (2005). The RNA binding protein TLS is translocated to dendritic spines by mGluR5 activation and regulates spine morphology. Curr. Biol. *15*, 587–593.

Gao, F.-B., and Taylor, J.P. (2014). RNA metabolism in neurological disease. Brain Res. *1584*, 1–2.

Gerstberger, S., Hafner, M., and Tuschl, T. (2014). A census of human RNA-binding proteins. Nat. Rev. Genet. *15*, 829–845.

Golumbeanu, M., Mohammadi, P., and Beerenwinkel, N. (2016). BMix: probabilistic modeling of occurring substitutions in PAR-CLIP data. Bioinformatics *32*, 976–983.

Groen, E.J.N., Fumoto, K., Blokhuis, A.M., Engelen-Lee, J., Zhou, Y., van den Heuvel, D.M.A., Koppers, M., van Diggelen, F., van Heest, J., Demmers, J.A.A., et al. (2013). ALS-associated mutations in FUS disrupt the axonal distribution and function of SMN. Hum. Mol. Genet. *22*, 3690–3704.

Hafner, M., Landthaler, M., Burger, L., Khorshid, M., Hausser, J., Berninger, P., Rothballer, A., Ascano, M., Jr., Jungkamp, A.-C., Munschauer, M., et al. (2010). Transcriptome-wide identification of RNA-binding protein and microRNA target sites by PAR-CLIP. Cell *141*, 129–141.

Hoell, J.I., Larsson, E., Runge, S., Nusbaum, J.D., Duggimpudi, S., Farazi, T.A., Hafner, M., Borkhardt, A., Sander, C., and Tuschl, T. (2011). RNA targets of wild-type and mutant FET family proteins. Nat. Struct. Mol. Biol. *18*, 1428–1431.

Ishigaki, S., Masuda, A., Fujioka, Y., Iguchi, Y., Katsuno, M., Shibata, A., Urano, F., Sobue, G., and Ohno, K. (2012). Position-dependent FUS-RNA interactions regulate alternative splicing events and transcriptions. Sci. Rep. *2*, 529.

Kapeli, K., Pratt, G.A., Vu, A.Q., Hutt, K.R., Martinez, F.J., Sundararaman, B., Batra, R., Freese, P., Lambert, N.J., Huelga, S.C., et al. (2016). Distinct and shared functions of ALS-associated proteins TDP-43, FUS and TAF15 revealed by multisystem analyses. Nat. Commun. *7*, 12143.

Kloetgen, A., Borkhardt, A., Hoell, J.I., and McHardy, A.C. (2016). The PARA-suite: PAR-CLIP specific sequence read simulation and processing. PeerJ *4*, e2619.

Kwiatkowski, T.J., Jr., Bosco, D.A., Leclerc, A.L., Tamrazian, E., Vanderburg, C.R., Russ, C., Davis, A., Gilchrist, J., Kasarskis, E.J., Munsat, T., et al. (2009). Mutations in the FUS/TLS gene on chromosome 16 cause familial amyotrophic lateral sclerosis. Science *323*, 1205–1208.

Lagier-Tourenne, C., Polymenidou, M., and Cleveland, D.W. (2010). TDP-43 and FUS/TLS: emerging roles in RNA processing and neurodegeneration. Hum. Mol. Genet. *19*, R46–R64.

Lagier-Tourenne, C., Polymenidou, M., Hutt, K.R., Vu, A.Q., Baughn, M., Huelga, S.C., Clutario, K.M., Ling, S.-C., Liang, T.Y., Mazur, C., et al. (2012). Divergent roles of ALS-linked proteins FUS/TLS and TDP-43 intersect in processing long pre-mRNAs. Nat. Neurosci. *15*, 1488–1497.

Lenzi, J., De Santis, R., de Turris, V., Morlando, M., Laneve, P., Calvo, A., Caliendo, V., Chiò, A., Rosa, A., and Bozzoni, I. (2015). ALS mutant FUS proteins are recruited into stress granules in induced pluripotent stem cell-derived motoneurons. Dis. Model. Mech. *8*, 755–766.

Li, H., and Durbin, R. (2010). Fast and accurate long-read alignment with Burrows-Wheeler transform. Bioinformatics *26*, 589–595.

Ling, S.-C., Polymenidou, M., and Cleveland, D.W. (2013). Converging mechanisms in ALS and FTD: disrupted RNA and protein homeostasis. Neuron *79*, 416–438.

Maatz, H., Kolinski, M., Hubner, N., and Landthaler, M. (2017). Transcriptome-wide Identification of RNA-binding Protein Binding Sites Using Photoactivatable-Ribonucleoside-Enhanced Crosslinking Immunoprecipitation (PAR-CLIP). Curr. Protoc. Mol. Biol. *118*, 27.6.1–27.6.19.

Mackenzie, I.R.A., Ansorge, O., Strong, M., Bilbao, J., Zinman, L., Ang, L.-C., Baker, M., Stewart, H., Eisen, A., Rademakers, R., and Neumann, M. (2011). Pathological heterogeneity in amyotrophic lateral sclerosis with FUS mutations: two distinct patterns correlating with disease severity and mutation. Acta Neuropathol. *122*, 87–98.

Martin, M. (2011). Cutadapt removes adapter sequences from high-throughput sequencing reads. EMBnet J. *17*, 10.

Masuda, A., Takeda, J., Okuno, T., Okamoto, T., Ohkawara, B., Ito, M., Ishigaki, S., Sobue, G., and Ohno, K. (2015). Position-specific binding of FUS to nascent RNA regulates mRNA length. Genes Dev. *29*, 1045–1057.

Morlando, M., Dini Modigliani, S., Torrelli, G., Rosa, A., Di Carlo, V., Caffarelli, E., and Bozzoni, I. (2012). FUS stimulates microRNA biogenesis by facilitating co-transcriptional Drosha recruitment. EMBO J. *31*, 4502–4510.

Nakaya, T., Alexiou, P., Maragkakis, M., Chang, A., and Mourelatos, Z. (2013). FUS regulates genes coding for RNA-binding proteins in neurons by binding to their highly conserved introns. RNA *19*, 498–509.

Neumann, M., Kwong, L.K., Lee, E.B., Kremmer, E., Flatley, A., Xu, Y., Forman, M.S., Troost, D., Kretzschmar, H.A., Trojanowski, J.Q., and Lee, V.M. (2009). Phosphorylation of S409/410 of TDP-43 is a consistent feature in all sporadic and familial forms of TDP-43 proteinopathies. Acta Neuropathol. *117*, 137–149.

Nishimoto, Y., Nakagawa, S., Hirose, T., Okano, H.J., Takao, M., Shibata, S., Suyama, S., Kuwako, K., Imai, T., Murayama, S., et al. (2013). The long non-coding RNA nuclear-enriched abundant transcript 1_2 induces paraspeckle formation in the motor neuron during the early phase of amyotrophic lateral sclerosis. Mol. Brain *6*, 31.

Patel, A., Lee, H.O., Jawerth, L., Maharana, S., Jahnel, M., Hein, M.Y., Stoynov, S., Mahamid, J., Saha, S., Franzmann, T.M., et al. (2015). A Liquid-to-Solid Phase Transition of the ALS Protein FUS Accelerated by Disease Mutation. Cell *162*, 1066–1077.

Prevedel, R., Diz-Muñoz, A., Ruocco, G., and Antonacci, G. (2019). Brillouin microscopy—a revolutionary tool for mechanobiology? arXiv, arXiv:1901.02006.

Quinlan, A.R., and Hall, I.M. (2010). BEDTools: a flexible suite of utilities for comparing genomic features. Bioinformatics *26*, 841–842.

Roehr, J.T., Dieterich, C., and Reinert, K. (2017). Flexbar 3.0—SIMD and multicore parallelization. Bioinformatics *33*, 2941–2942.

Rogelj, B., Easton, L.E., Bogu, G.K., Stanton, L.W., Rot, G., Curk, T., Zupan, B., Sugimoto, Y., Modic, M., Haberman, N., et al. (2012). Widespread binding of FUS along nascent RNA regulates alternative splicing in the brain. Sci. Rep. *2*, 603.

Rosa, A., Papaioannou, M.D., Krzyspiak, J.E., and Brivanlou, A.H. (2014). miR-373 is regulated by TGFβ signaling and promotes mesendoderm differentiation in human Embryonic Stem Cells. Dev. Biol. *391*, 81–88.

Sances, S., Bruijn, L.I., Chandran, S., Eggan, K., Ho, R., Klim, J.R., Livesey, M.R., Lowry, E., Macklis, J.D., Rushton, D., et al. (2016). Modeling ALS with motor neurons derived from human induced pluripotent stem cells. Nat. Neurosci. *19*, 542–553.

Scarcelli, G., Polacheck, W.J., Nia, H.T., Patel, K., Grodzinsky, A.J., Kamm, R.D., and Yun, S.H. (2015). Noncontact three-dimensional mapping of intracellular hydromechanical properties by Brillouin microscopy. Nat. Methods *12*, 1132–1134.

Scheckel, C., Drapeau, E., Frias, M.A., Park, C.Y., Fak, J., Zucker-Scharff, I., Kou, Y., Haroutunian, V., Ma'ayan, A., Buxbaum, J.D., and Darnell, R.B. (2016). Regulatory consequences of neuronal ELAV-like protein binding to coding and non-coding RNAs in human brain. eLife *5*, e10421.

Tebaldi, T., Zuccotti, P., Peroni, D., Köhn, M., Gasperini, L., Potrich, V., Bonazza, V., Dudnakova, T., Rossi, A., Sanguinetti, G., et al. (2018). HuD Is a Neural Translation Enhancer Acting on mTORC1-Responsive Genes and Counteracted by the Y3 Small Non-coding RNA. Mol. Cell *71*, 256–270.e10.

Udagawa, T., Fujioka, Y., Tanaka, M., Honda, D., Yokoi, S., Riku, Y., Ibi, D., Nagai, T., Yamada, K., Watanabe, H., et al. (2015). FUS regulates AMPA receptor function and FTLD/ALS-associated behaviour via GluA1 mRNA stabilization. Nat. Commun. *6*, 7098.

Van Deerlin, V.M., Leverenz, J.B., Bekris, L.M., Bird, T.D., Yuan, W., Elman, L.B., Clay, D., Wood, E.M., Chen-Plotkin, A.S., Martinez-Lage, M., et al. (2008). TARDBP mutations in amyotrophic lateral sclerosis with TDP-43 neuropathology: a genetic and histopathological analysis. Lancet Neurol. *7*, 409–416.

Vance, C., Rogelj, B., Hortobágyi, T., De Vos, K.J., Nishimura, A.L., Sreedharan, J., Hu, X., Smith, B., Ruddy, D., Wright, P., et al. (2009). Mutations in FUS, an RNA processing protein, cause familial amyotrophic lateral sclerosis type 6. Science *323*, 1208–1211.

Wang, X., Arai, S., Song, X., Reichart, D., Du, K., Pascual, G., Tempst, P., Rosenfeld, M.G., Glass, C.K., and Kurokawa, R. (2008). Induced ncRNAs allosterically modify RNA-binding proteins in cis to inhibit transcription. Nature *454*, 126–130.

Wolozin, B. (2012). Regulated protein aggregation: stress granules and neurodegeneration. Mol. Neurodegener. *7*, 56.

Yokoi, S., Udagawa, T., Fujioka, Y., Honda, D., Okado, H., Watanabe, H., Katsuno, M., Ishigaki, S., and Sobue, G. (2017). 3'UTR Length-Dependent Control of SynGAP Isoform $\alpha 2$ mRNA by FUS and ELAV-like Proteins Promotes Dendritic Spine Maturation and Cognitive Function. Cell Rep. *20*, 3071–3084.

Yokoseki, A., Shiga, A., Tan, C.-F., Tagawa, A., Kaneko, H., Koyama, A., Eguchi, H., Tsujino, A., Ikeuchi, T., Kakita, A., et al. (2008). TDP-43 mutation in familial amyotrophic lateral sclerosis. Ann. Neurol. *63*, 538–542.

Zhou, Y., Liu, S., Liu, G., Oztürk, A., and Hicks, G.G. (2013). ALS-associated FUS mutations result in compromised FUS alternative splicing and autoregulation. PLoS Genet. *9*, e1003895.

STAR★METHODS

KEY RESOURCES TABLE

REAGENT or RESOURCE	SOURCE	IDENTIFIER
Antibodies		
Mouse monoclonal anti FUS/TLS antibody	Santa Cruz Biotechnology	Cat#sc-47711; RRID: AB_2105208
Mouse monoclonal anti-phospho TDP-43 pS409/410 antibody	Cosmo Bio	Cat#TIP-PTD-M01; RRID: AB_1961900
Mouse monoclonal anti-HuD antibody (E-1)	Santa Cruz Biotechnology	Cat#sc-28299; RRID: AB_627765
Mouse monoclonal anti-ELAVL4 antibody	Santa Cruz Biotechnology	Cat#sc-48421; RRID: AB_627766
Goat polyclonal anti-Actin antibody	Santa Cruz Biotechnology	Cat#sc-1616; RRID: AB_630836
Mouse monoclonal anti-FLAG M2 antibody	Sigma-Aldrich	Cat#F1804; RRID: AB_262044
Rabbit polyclonal anti-FUS/TLS antibody	Abcam	Cat#AB84078; RRID: AB_2105201
Mouse monoclonal anti-Islet-1/2 antibody	DSHB	Cat#39.4D5; RRID: AB_2314683
Mouse monoclonal anti-PABP antibody	Santa Cruz Biotechnology	Cat#SC-32318; RRID: AB_628097
Goat polyclonal anti-TIAR antibody	Santa Cruz Biotechnology	Cat#SC-1749; RRID: AB_632508
Rabbit polyclonal anti-TUJ1 antibody	Sigma-Aldrich	Cat#T2200; RRID: AB_262133
Goat anti-mouse Alexa Fluor 488 antibody	Immunological Sciences	Cat#IS-20010; RRID: AB_10559812
Donkey anti-rabbit Alexa Fluor 594 antibody	Immunological Sciences	Cat#IS-20152-1; RRID: AB_10853603
Donkey anti-goat Alexa Fluor 594 antibody	Immunological Sciences	Cat#IS-20116-1; RRID: AB_10853466
Donkey anti-mouse Alexa Fluor 647 antibody	Life Technologies	Cat#A31571; RRID: AB_162542
Mouse monoclonal anti-alpha-TUBULIN antibody	Sigma-Aldrich	Cat#T6199; RRID: AB_477583
Goat polyclonal anti-LAMIN B antibody	Santa Cruz Biotechnology	Cat#sc-6216; RRID: AB_648156
Mouse monoclonal ANTI-FLAG(R) M2-Peroxidase (HRP) antibody	Sigma-Aldrich	Cat#A8592; RRID: AB_439702
Mouse monoclonal HA-probe (F-7) antibody	Santa Cruz Biotechnology	Cat#sc-7392; RRID: AB_627809
Biological Samples		
Patients' spinal cord spacimen, see Tables S2 and S3	This paper	N/A
Chemicals, Peptides, and Recombinant Proteins		
SU-5402	Sigma-Aldrich	SML0443-5MG
poly-L-ornithine	Sigma-Aldrich	Cat#P4957-50ML
laminin	Sigma-Aldrich	Cat#L2020-1MG
4-thiouridine	Sigma-Aldrich	Cat#T4509
T4 RNA ligase 2, Rnl2(1–249) K227Q ligase	New England Biolabs	Cat#M0351L
Lipofectamine 2000	Life Technologies	Cat#11668030
doxycycline	Sigma-Aldrich	Cat#D9891-1G
DAPI	Sigma-Aldrich	Cat#D9542-1MG
all-trans retinoic acid	Sigma-Aldrich	Cat#R2625
SAG	Merck Millipore	Cat#566660
SB431542	Miltenyi Biotec	Cat#130-106-275
LDN-193189	Miltenyi Biotec	Cat#130-106-540
DAPT	Sigma-Aldrich	Cat#D5942
Critical Commercial Assays		
Dual Glo luciferase assay	Promega	Cat#E2920
Vector Blue alkaline phosphatase substrate kit III	Vector laboratories Inc.	Cat#SK-5300
Quick-RNA MiniPrep	Zymo Research	Cat#R1054
PrimeScript RT-PCR Kit	Takara Scientific	Cat#RR014B
SYBR Green PowerUP	Thermo Fisher Scientific	Cat#A25742

(*Continued on next page*)

Continued

REAGENT or RESOURCE	SOURCE	IDENTIFIER
Deposited Data		
PAR-CLIP raw data	This paper	GEO: GSE118347
Experimental Models: Cell Lines		
iPSC line FUS^{WT}	Lenzi et al., 2015	N/A
iPSC line FUS^{P525L}	Lenzi et al., 2015	N/A
HeLa cell line	ATCC	HeLa
Oligonucleotides		
Primer RLuc FW: TCGTCCATGCTGAGAGTGTC	This paper	N/A
Primer RLuc REV: CTAACCTCGCCCTTCTCCTT	This paper	N/A
Primer FLuc FW: TGCAGAAGATCCTGAACGTG	This paper	N/A
Primer FLuc REV: CGGTAGACCCAGAGCTGTTC	This paper	N/A
Primer ATP5O FW: ACTCGGGTTTGACCTACAGC	This paper	N/A
Primer ATP5O RV: GGTACTGAAGCATCGCACCT	This paper	N/A
Primer ELAVL4 FW: CAACCCCAGCCAGAAGTCCA	This paper	N/A
Primer ELAVL4 RV: AGCCTGAACCTCTGAGCCTG	This paper	N/A
Primer ISL-1 FW: TACAAAGTTACCAGCCACC	This paper	N/A
Primer ISL-1 RV: GGAAGTTGAGAGGACATTGA	This paper	N/A
Recombinant DNA		
ELAVL4 plasmid, pFRT-TODestFLAGHA_HuD	Thomas Tuschl	Addgene #65757; RRID: Addgene_65757
Plasmid epB-Puro-TT-RFP	Rosa et al., 2014	N/A
pSI-Check2 vector	Promega	Cat#C8021; RRID: Addgene_106979
Plasmid epB-Puro-TT-RFP-FUS	This paper	N/A
Plasmid epB-Puro-TT-RFP-FUS-P525L	This paper	N/A
Plasmid epB-Bsd-TT-GFP-ELAVL4	This paper	N/A
Software and Algorithms		
Huygens Professional version 18.04, Deconvolution software	Scientific Volume Imaging	https://svi.nl/Huygens-Professional
Imaris 8.1.2, 3D quantitative analysis software	Bitplane Scientific Software	http://www.bitplane.com/releasenotes/imaris812.aspx
Flexbar, Demultiplexing software	Roehr et al., 2017	https://github.com/seqan/flexbar
Cutadapt, adaptor trimming software	Martin, 2011	https://cutadapt.readthedocs.io/en/stable/index.html
FASTX Trimmer, Command line tools for Short-Reads FASTA/FASTQ files preprocessing	Hannon lab	http://hannonlab.cshl.edu/fastx_toolkit/
PARA-Suite aligner, Sequence alignment software	Kloetgen et al., 2016	https://github.com/akloetgen/PARA-suite_aligner
BMix tool, PAR-CLIP analysis tool	Golumbeanu et al., 2016	https://omictools.com/bmix-tool
BEDTools suite, PAR-CLIP analysis tool	Quinlan and Hall, 2010	https://bedtools.readthedocs.io/en/latest/index.html
CASAVA package, Sequencing data analysis tool	Illumina	https://www.illumina.com/
Portal for the analysis of gene expression in human tissues	Genotype-Tissue Expression (GTEx) Portal Version 7	https://www.gtexportal.org/home/

CONTACT FOR REAGENT AND RESOURCE SHARING

Further information and requests for resources and reagents should be directed to and will be fulfilled by the Lead Contact, Alessandro Rosa (alessandro.rosa@uniroma1.it).

EXPERIMENTAL MODEL AND SUBJECT DETAILS

Human iPSC lines

Derivation and maintenance conditions of human iPSCs carrying the P525L mutation in both *FUS* alleles (FUS^{P525L}, male) and their isogenic *FUS* wild-type control (FUS^{WT}, male) used in this study are described in Lenzi et al. (2015). The MN differentiation protocol is detailed in De Santis et al. (2017) and depicted in Figure S1A. In brief, cells were differentiated in N2B27 medium supplemented with 1 mM all-trans retinoic acid (Sigma-Aldrich) and 1 mM SAG (Merck Millipore) for 12 days in the presence of 10 mM SB431542 and 100 nM LDN-193189 (both from Miltenyi Biotec) from day 0 to 6, and 5 mM DAPT and 4 mM SU-5402 (both from Sigma-Aldrich) from day 6 to 12. Cells were sorted at day 12-13 using a FACSAria III (BD Biosciences) and re-plated on poly-L-ornithine- and laminin-coated dishes (both from Sigma-Aldrich) in Neural Medium as described in De Santis et al. (2017).

HeLa cells

HeLa cells were purchased from ATCC and maintained in DMEM-F12 supplemented with 10% FBS, 1x Penicillin/Streptomycin (all from Sigma-Aldrich) and 1x Glutamax (Life Technologies).

Spinal cord samples from ALS patients

Consent for autopsy was obtained in concordance with institutional regulations. Patient and control details are included in Tables S2 and S3.

METHOD DETAILS

PAR-CLIP analysis

iPSC-derived motor neurons (day 12+3 of differentiation, see Figure S1A) were cultured in presence of 400 μM 4-thiouridine (Sigma-Aldrich) for 8 hours. UV crosslinking at 365 nm was performed at 0.15 J/cm2 with a CL-1000 Ultraviolet Crosslinker (UVP), in PBS. Cell pellets were then resuspended in NP40 lysis buffer (50 mM HEPES-KOH, 150 mM KCl, 2 mM EDTA, 1 mM NaF, 0.5% (v/v) NP40, 0.5 mM DTT and complete EDTA-free protease inhibitor cocktail) and incubated for 15 minutes on ice. Both FUS-WT and FUS-P525L IP were performed using anti-FUS/TLS antibody (sc-47711, Santa Cruz Biotechnology) for 2 hours at 4°C in NP40 lysis buffer. Ectopically expressed FLAG-FUS-WT and FLAG-FUS-P525L IP was performed using anti-FLAG M2 antibody (F1804, Sigma-Aldrich) for 1 hour at 4°C in NP40 lysis buffer. The PAR-CLIP was carried out as previously described (Maatz et al., 2017) with exception of 3′ Adaptor ligation that was performed on beads after immunoprecipitation (Benhalevy et al., 2017). Briefly, beads-Ab after IP for FUS were washed with 1X RNA ligase buffer without ATP (New England Biolabs) two times and then incubated with a reaction mixture for the ligation of the 3′ adenylated adaptor composed of 1X RNA ligase buffer without ATP, 15% aqueous PEG-8000, 2 μM adenylated 3′ adaptor oligonucleotide and 200 U of Rnl2(1–249) K227Q ligase (New England Biolabs). Sequencing was performed on an Illumina HiSeq4000 using 51 cycles to obtain 20 to 55 million raw reads. Sequencing data was converted using the bcl2fastq tool from the Illumina CASAVA package, followed by demultiplexing and 3′ adaptor trimming using Flexbar (Roehr et al., 2017) and Cutadapt (Martin, 2011) software, respectively. To remove PCR duplicates, reads with identical sequence were collapsed, then we used FASTX Trimmer tool (http://hannonlab.cshl.edu/fastx_toolkit/) to remove random nucleotides from both ends of collapsed reads. Reads shorter than 14 nucleotides were discarded. BWA-based (Li and Durbin, 2010) PARA-Suite aligner (Kloetgen et al., 2016) was used to align reads to GRCh38 genome and to a custom database of exon-exon junctions generated from Ensembl 89 transcriptome annotation (Aken et al., 2017). We handled multi-mapping reads by keeping only those that mapped once with at least one T-C mismatch: mapping positions indicating T-C transitions were chosen as the correct ones. Cross-link induced T-C transitions were called for each individual replicate using BMix tool (Golumbeanu et al., 2016). To evaluate the consistency of biological replicates we calculated a distance score for each pair of samples equal to the number of T-C transitions not in common over the total number of T-C transitions, found using the BEDTools intersect tool (Quinlan and Hall, 2010). Similarity between replicates was confirmed by distance score-based hierarchical clustering of samples (Figure S1). This similarity prompted us to combine alignment files from each pair of replicates and repeat T-C transition calling on the resulting files in order to increase sensitivity. Only transitions supported by at least two reads from both replicates were kept.

Plasmid construction and transfection

The epB-Puro-TT-RFP, epB-Puro-TT-RFP-FUS, epB-Puro-TT-RFP-FUS-P525L and epB-Bsd-TT-GFP-ELAVL4 were generated by inserting the transgene sequences in the enhanced piggyBac transposable vector (Rosa et al., 2014). ELAVL4 coding sequence was obtained from the pFRT-TODestFLAGHA_HuD plasmid (Addgene#65757). The resulting constructs contain the enhanced piggyBac terminal repeats flanking a constitutive cassette driving the expression of the blasticidin or puromycin resistance genes fused to the rtTA gene and, in the opposite direction, a tetracycline-responsive promoter element (TRE) driving the conditional expression of the transgenes. HeLa cells were co-transfected with 4.5 μg of transposable vector and 0.5 μg of the piggyBac transposase using Lipofectamine 2000 (Life Technologies) following manufacturer's instructions. Selection with 5 μg/ml blasticidin or 0.5 μg/mL puromycin gave rise to stable and inducible cell lines. For transgene induction, 200 ng/ml of doxycycline (Sigma-Aldrich) were added to the medium 24 hours before the analysis.

Luciferase assay

Target 3′UTRs were cloned in the pSI-Check2 vector. Reporter vectors were transfected in 50,000 pre-seeded HeLa cells in a 24-well plate using Lipofectamine 2000 (Life Technologies) following manufacturer's instructions. Cells were harvested 24 hours post-transfection and RLuc and FLuc activities were measured by Dual Glo luciferase assay (Promega) according to the manufacturer's protocol. An aliquot of cell lysate was kept for RNA extraction and checked by RT-PCR with primers annealing to RLuc and FLuc sequences (RLuc FW: TCGTCCATGCTGAGAGTGTC; RLuc REV: CTAACCTCGCCCTTCTCCTT; FLuc FW: TGCAGAAGATCCT GAACGTG; FLuc REV: CGGTAGACCCAGAGCTGTTC).

Co-immunoprecipitation

Cytoplasmic fractionation was performed in HeLa cells and iPSC-derived MNs using a NP40 hypotonic buffer (HEPES-KOH 10mM, EDTA 0.1mM, 0.5% (v/v) NP40, KCl 10mM, DTT 1mM and complete EDTA-free protease inhibitor cocktail) for 15 minutes on ice. Supernatant was considered cytoplasmic extract, while pellet nuclei. Salt concentration was equilibrated using a 2X NP40 buffer. Pre-cleaning of cytoplasmic extract was performed by 30 minutes incubation with Protein G magnetic beads (Life Technologies). Immunoprecipitation was performed using 5 μg of FUS antibody (sc-47711; Santa Cruz Biotechnology) for 1h at 4°C. Samples were washed 3 times using NP40 buffer and protein complex were released by resuspending the beads in LDS buffer 1X (Life Technologies) for 5′ at 95°C.

Immunostaining

Cells seeded on μ-slide 8-well (ibidi) were washed twice with PBS, fixed in 4% paraformaldehyde for 15 minutes at room temperature and then incubated for 5 minutes in 0.1M glycine. Fixed cells were then permeabilized with PBS containing 0.05% Triton X-100 for 5 minutes and subsequently incubated for 20 minutes with antibody blocking solution (ABS: 3% BSA in PBS). Primary antibodies were incubated overnight at 4°C. The primary antibodies used are: anti-FUS/TLS (Abcam, AB84078; 1:100), anti-Islet-1/2 (DSHB, 39.4D5; 1:50), anti-PABP (Santa Cruz Biotechnology, SC-32318; 1:100), anti ELVL4/HuD (Santa Cruz Biotechnology, SC-48421, 1:100) and anti-TIAR (Santa Cruz Biotechnology, SC-1749; 1:50), anti-TUJ1 (Sigma-Aldrich, T2200, 1:2000). The secondary antibodies were diluted 1:250 in ABS and incubated for 1 hour at room temperature. The secondary antibodies are: anti-mouse Alexa Fluor 488 (Immunological Sciences, IS-20010), anti-rabbit Alexa Fluor 594 (Immunological Sciences, IS-20152-1), anti-goat Alexa Fluor 594 (Immunological Sciences, IS-20116-1) and anti-mouse Alexa Fluor 647 (Life Technologies, A31571). 0.4 μg/ml DAPI (Sigma-Aldrich) was used for 5 minutes to label nuclei. Cells were then mounted using ibidi Mounting Medium (ibidi). Double fluorescent-labeling on spinal cord samples from FUS ALS patients were performed as previously described (Blokhuis et al., 2016); sections were analyzed using a Zeiss LSM 880 laser scanning confocal microscope.

Image acquisition, deconvolution and analysis

Confocal images of Figures 1, 2, 3, and 4 were acquired at the Olympus iX83 FluoView1200 laser scanning confocal microscope using a 60x NA1.35 oil objective and 405nm, 473nm and 559nm lasers. Filter setting for DAPI, Alexa Fluor 488 and Alexa Fluor 594 were used. For ELAVL4 signal quantification, the raw stack images were first deconvolved with Huygens Professional version 18.04 (Scientific Volume Imaging, the Netherlands, https://svi.nl), using the CMLE algorithm, with SNR:15 and 50 iterations. Then 3D quantitative analysis was performed using Surfaces in Imaris 8.1.2 (Bitplane Scientific Software, USA), mean intensity and volume values of each speckle or stress granule were exported in Prism 7 for statistical analysis and graph display.

Immunohistochemistry

For immunohistochemistry on human spinal cord samples from sporadic ALS patients, formalin-fixed paraffin-embedded 6 μm thick sections were deparaffinized in xylene and rinsed in graded ethanol (100%, 95%, 70%). Antigen retrieval was performed in citrate buffer (10 mM sodium citrate, pH 6.0) at 120°C for 10 minutes using a pressure cooker followed by incubation with a given primary antibody (mouse anti-phospho TDP-43 pS409/410, TIP-PTD-M01, Cosmo Bio, Tokyo, Japan; 1:2.500). Due to antibody incompatibilities we were unable to perform double fluorescent-labeling. For double immunohistochemistry, sections were incubated with Brightvision rabbit-anti-mouse for 15 min at RT and subsequently with poly-horseradish peroxidase-anti-rabbit (Immunologic, Duiven, the Netherlands) for 30 min at RT, and washed with PBS. Horseradish peroxidase was visualized with filtered $5x10^{-4\%}$ w/v AEC in in 0.05 M acetate buffer pH 4,9 and $1x10^{-4\%}$ H_2O_2. To remove the first primary antibody, sections were incubated at 120°C in citrate buffer for 10 min. Incubation with mouse anti-HuD antibody (E-1, sc-28299, Santa Cruz Biotechnology, CA, USA; 1:50) was performed overnight at 4°C. The next day the sections were incubated with Brightvision poly-alkaline phosphatase- goat-anti mouse (Immunologic, Duiven, the Netherlands) for 30 min at RT and washed with PBS. Sections were washed with Tris–HCl buffer (0.1 M, pH 8.2) to adjust the pH. Alkaline phosphatase activity was visualized with the Vector Blue alkaline phosphatase substrate kit III (SK-5300, Vector laboratories Inc., CA, USA) Sections incubated without primary antibodies or with heat-inactivated primary antibodies were blank.

BDB microscopy

HeLa cells (50,000) were seeded in each μ-Dish 35 mm high Grid-50 Glass Bottom (Ibidi) in 2 mL of culture medium. Doxycycline (200 ng/ml; Sigma-Aldrich) was added to the medium for ectopic protein induction. The next day, cells were prepared as follows: washed with PBS (Sigma-Aldrich), fixed with 4% paraformaldehyde for 15 minutes at room temperature, washed with PBS, incubated 5 minutes with PBS containing 0.1M glycine, washed 2 times with PBS and left in PBS for confocal and Brillouin acquisition, as previously described (Antonacci et al., 2018). For the analysis shown in Figure 3E, a mask on portions of the cytoplasm showing high fluorescent signal was first created to localize different subcellular regions across the associated Brillouin images, in turn providing a measure of the frequency shift (a stiffness indicator).

Gene expression analysis

Total RNA, extracted with the Quick-RNA MiniPrep (Zymo Research) and retrotranscribed with PrimeScript (Takara Scientific), was analyzed by real-time qRT-PCR with SYBR Green PowerUP (Thermo Fisher Scientific) as previously described (De Santis et al., 2017). *ATP5O* was used as the internal calibrator. Primers sequences are ATP5O FW: ACTCGGGTTTGACCTACAGC; ATP5O RV: GGTACTGAAGCATCGCACCT; ELAVL4 FW: CAACCCCAGCCAGAAGTCCA; ELAVL4 RV: AGCCTGAACCTCTGAGCCTG; ISL-1 FW: TACAAAGTTACCAGCCACC; ISL-1 RV: GGAAGTTGAGAGGACATTGA. Western blot analysis was carried out using anti-ELAVL4 (sc-48421; Santa Cruz Biotechnology), anti-FUS (sc-47711; Santa Cruz Biotechnology), anti-Actin (sc-1616; Santa Cruz Biotechnology), anti-FLAG-HRP (F7425; Sigma-Aldrich) primary antibodies and anti-HA-HRP (sc-7392; Santa Cruz Biotechnology) secondary antibody, as previously described (Lenzi et al., 2015).

The Genotype-Tissue Expression (GTEx) Project was supported by the Common Fund of the Office of the Director of the National Institutes of Health, and by NCI, NHGRI, NHLBI, NIDA, NIMH, and NINDS. The data used for the analyses described in this manuscript were obtained from the GTEx Portal (https://www.gtexportal.org/home/), Version 7, on 07/31/18.

QUANTIFICATION AND STATISTICAL ANALYSIS

All the statistical details of experiments (including the statistical tests used, exact value of n, what n represents, definition of center, dispersion and precision measures) can be found in the figure legends.

DATA AVAILABILITY

The accession number for the PAR-CLIP raw data reported in this paper is GEO: GSE118347